MECHANICAL STRENGTH OF 3D PRINTED OBJECTS:

EXPERIMENTAL AND NUMERICAL INVESTIGATION

A THESIS SUBMITTED TO
THE GRADUATE SCHOOL OF NATURAL AND APPLIED SCIENCES
OF
MIDDLE EAST TECHNICAL UNIVERSITY

BY

GÖZDE BAŞARA

IN PARTIAL FULFILLMENT OF THE REQUIREMENTS
FOR
THE DEGREE OF MASTERS OF SCIENCE
IN
MECHANICAL ENGINEERING

JULY 2017

Approval of the thesis:

MECHANICAL STRENGTH OF 3D PRINTED OBJECTS:

EXPERIMENTAL AND NUMERICAL INVESTIGATION

submitted by **GÖZDE BAŞARA** in partial fulfillment of the requirements for the degree of the **Master of Science in Mechanical Engineering Department, Middle East Technical University** by,

Prof. Dr. Gülbin Dural Ünver _____
Dean, Graduate School of **Natural and Applied Sciences**

Prof. Dr. Tuna Balkan _____
Head of Department, **Mechanical Engineering**

Prof. Dr. İlker Tarı _____
Supervisor, **Mechanical Engineering Dept., METU**

Examining Committee Members:

Asst. Prof. Dr. Özgür Bayer _____
Mechanical Engineering Dept., METU

Prof. Dr. İlker Tarı _____
Mechanical Engineering Dept., METU

Asst. Prof. Dr. Ulaş Yaman _____
Mechanical Engineering Dept., METU

Prof. Dr. Cemal Niyazi Sökmen _____
Nuclear Engineering Dept., Hacettepe University

Prof. Dr. Cemil Kocar _____
Nuclear Engineering Dept., Hacettepe University

Date: 20/07/2017

I hereby declare that all information in this document has been obtained and presented in accordance with academic rules and ethical conduct. I also declare that, as required by these rules and conduct, I have fully cited and referenced all material and results that are not original to this work.

Name, Last name: Gözde Başara

Signature :

ABSTRACT

MECHANICAL STRENGTH OF 3D PRINTED OBJECTS: EXPERIMENTAL AND NUMERICAL INVESTIGATION

Başara, Gözde

M.Sc., Department of Mechanical Engineering

Supervisor: Prof. Dr. İlker Tarı

July 2017, 102 pages

The number of people and the industries that are using 3 Dimensional (3D) printing increases everyday; however, the home-use of 3D printing remains below expectations partially due to limitation in the printer size. Many different technologies can be used in 3D printing. In this study Fused Deposition Modelling (FDM) is used. This method is commonly used for home-use 3D printing. In FDM, there is a wide range of materials that can be used and for this study the material is chosen as Poly Lactic Acid (PLA) being one of the most commonly used materials. In this study, to understand the mechanical behavior of the used material, compression and tensile tests are performed and they are verified numerically. The compression tests are done for two infill percentages of the parts and the results are compared. 100% infill parts show better mechanical properties than parts having 20% infill. Tensile tests are done

by using a whole specimen and two half specimens which are joined in the middle by using an adhesive. As a result, the difference in performance is observed. Glued specimens show lower performance. Afterwards, by using the results of the experiments numerical analyses are done. For the numerical analyses, ANSYS is used. The numerical results show consistency with the experimental results. Lastly, a case study is performed. In this case study, the effect of partitioning and joining the parts by using an adhesive, on the strength of the object is investigated for a motorcycle helmet. PLA was chosen as the material of the helmet and experimental results of PLA are used as the mechanical properties of the helmet. The results of whole helmet and partitioned helmet show similarity with a small difference under the same loading conditions. The stress results and the distribution of the stresses within the two helmets are also close to each other.

Keywords: 3D Printing, Fused Deposition Modelling, PLA, Mechanical Properties, Mechanical Stresses, Numerical Analysis

ÖZ

3 BOYUTLU YAZICILARDA ÜRETİLMİŞ NESNELERİN MEKANİK DAYANIMI: DENEYSEL VE NUMERİK İNCELEME

Başara, Gözde

Yüksek Lisans, Makina Mühendisliği Bölümü

Tez Yöneticisi: Prof. Dr. İlker Tarı

Temmuz 2017, 102 sayfa

3 Boyutlu (3B) yazıcıların kullanıldığı alanlar ve kullanıcı insan sayısı günden güne artıyor; ancak ev tipi 3B yazıcıların kullanımı yazıcı boyutlarının küçük olması nedeniyle beklentilerin altında kalmaktadır. 3B yazıcılarda pek çok değişik teknoloji kullanılabilir. Bu çalışmada, Eriyik Yığma Modelleme (EYM) kullanılmıştır. Bu method yaygın olarak ev tipi 3B yazıcılarda kullanılmaktadır. EYM de çok sayıda farklı malzeme kullanılabilir ve bu çalışmada, kullanımı en yaygın malzemelerden biri olan Poli Laktik Asit (PLA) kullanılmıştır. Bu çalışmada, kullanılan malzemenin mekanik özelliklerini anlamak için basma ve çekme testleri yapılmış, numerik olarak da doğrulanmıştır. Basma testleri, içi farklı yüzdelerde dolu olan parçalarla yapılmış ve sonuçlar kıyaslanmıştır. İçi 100% dolu olan parçalar, içi %20 dolu olan parçalara göre daha iyi mekanik özellikler göstermiştir. Çekme testleri öncelikle bütün bir parça

numunesi için, daha sonra ortadan bölünmüş ve yapıştırılmış iki yarım parça numunesi için yapılmış olup aralarındaki performans farkı gözlenmiştir. Yapıştırılan parça numunesi daha düşük performans göstermiştir. Deneylerin tamamlanması sonrasında, deney sonuçları kullanılarak numerik analizler yapılmıştır. Bu amaçla ANSYS kullanılmıştır. Numerik analiz sonuçları deney sonuçları ile uyumludur. Son olarak, bir örnek çalışma yapılmıştır. Bu örnek çalışma motorsiklet kaskı için yapılmıştır. Kask parçalara ayrılıp yapıştırılarak bu işlemin kaskın dayanıklılığına etkisi incelenmiştir. Kask malzemesi olarak PLA seçilmiş ve PLA için bulunan deneysel sonuçlar kaskın mekanik özellikleri olarak kullanılmıştır. Bütün kask ve parçalanıp yapıştırılmış kask aynı yük altında benzer sonuçlar göstermiş olup, stres sonuçları ve stres dağılımları da benzerdir.

Anahtar Kelimeler: 3B Basma, Eriyik Yığma Modelleme, PLA, Mekanik Özellikler, Mekanik Stresler, Numerik analiz

To my family…

ACKNOWLEDGEMENTS

I would like to express my deepest gratitude to my supervisor Prof. Dr. İlker Tarı for his guidance. Throughout my master study I have felt his support and his effort to make me a better version of me. I am proud to be his student. I am also grateful to Prof. Dr. Sibel Tarı who conduced me to meet my thesis topic.

I would like to thank Servet Şehirli who helped me a lot with the experiments and answered my endless questions. I would like to express my special thanks to Alp Esin who I met as a result of a serendipity and learned a lot. I would like to thank Hüseyin Enes Salman for his help through the printing process. I am also thankful to Asst. Prof. Ulaş Yaman for sharing his experience in 3D printing.

I would like to thank my family for being so supportive and giving me encouraging talks when I needed. It was a pleasure to be a part of this family consisting of three mechanical engineers graduated from METU.

Away from work, I would like to thank my best friends İrem Velibeyoğlu and Ceren Cindioğlu. Their support was far beyond words. I would like to thank Eylül Şimşek for the chats. I would like to thank my colleague Burcu Karagöz for her friendship and helps. I would like to thank the Zumba crew in METU for boosting my energy. I would like to thank Ercan Karakoyunlu for his friendship and support.

This work is partially funded by Scientific and Technological Research Council of Turkey under grant number TÜBİTAK 112E208.

TABLE OF CONTENTS

LIST OF FIGURES

FIGURES

LIST OF TABLES

TABLES

NOMENCLATURE

Symbols		
A	Area	mm^2
F	Force	N
x	Deflection	mm
Greek Symbols		
σ	Standard deviation	-
μ	Mean	-
ρ	Density	-
Subscripts		
efs	Elastic foundation stifness	
Abbreviations		
3D	3 Dimensional	
502CAE	502 Cyanoarylate adhesive evobond	
ABS	Acrylonitrile butadiene styrene	
BSP	Binary space partitioning	
CAD	Computer aided drawing	
CLT	Classical laminate theory	
DIC	Digital image correlation	
EBM	Electron beam melting	
EFS	Elastic foundation stiffness	
EPS	Expanded polystyrene	
ESPI	Electronic speckle pattern interferometry	
FBG	Fiber Bragg grating	
FD	Fused deposited	

FDM	Fused deposition modelling
FEA	Finite element analysis
PC	Polycarbonate
PEEK	Polyether-ether-kethone
PLA	Poly lactic acid
RP	Rapid prototyping
SLM	Selective laser melting
SLS	Selective laser sintering
STL	Stereolithography
TLCP	Thermotropic liquid crystalline polymer

CHAPTER 1

INTRODUCTION

3D printing (additive manufacturing) technology has developed since the late 1970s when the first three-dimensional object was built by Swainson [1]. With the emergence of 3D printing, the traditional understanding of manufacturing, which is to manufacture by removing material, has changed into manufacturing by adding material [2]. By using 3D printing, an object is built by constructing layers successively. These layers are formed in such a way that the object gets its final shape in the end.

The number of people and the industries that are using 3D printing increases everyday. In some cases, 3D printing is more beneficial than traditional manufacturing for some reasons. Firstly, complex parts can be produced easily. Secondly, in 3D printing objects are created by adding layer upon layer. Therefore, prior to the manufacturing process, there is no need to design and manufacture tools. This makes 3D printing cheaper than some of the traditional manufacturing methods [3].

Many different technologies are used in 3D printing. Some of them are: Fused deposition modeling (FDM), selective laser melting (SLM), selective laser sintering (SLS), electron beam melting (EBM) and ink-jet printing [4]. Considering the scope of this study, among these technologies only FDM technology will be elaborated on. FDM is one of the most preferred rapid prototyping techniques since it is easy to operate, environmentally friendly, reproducible and it hardly forms waste material [5]. The most commonly used materials in FDM method are Acrylonitrile butadiene

styrene (ABS) and polylactic acid (PLA), polycarbonate, polyethylene and polypropylene [4].

In general, the first step of FDM is to create a model by using a CAD software. This model is then exported to a common data exchange format, for which STL (Stereolithography) is used frequently. Then, the model is broken into slices in order to form 2D lines. In the last step, the deposition path is created and then this data is sent to the FDM 3D printer. These steps are illustrated in Figure 1. Following the sets of four steps of preparation, printing process starts. During this process, FDM 3D printer creates tool paths. Based on these tool paths, the head moves in x-y plane and pours the melted material according to the desired geometry. The material, which is called filament, is solid at the beginning. It is piled by rolling and moved to an extrusion head where it is heated until a half-liquid state is reached. Then, through the nozzle, it is poured on the platform to construct the very thin first layer of the desired object. This layer solidifies almost immediately. To build the second layer, the platform is moved down in the z-axis. Then, layer upon layer, the desired object is built. After the printing process, the part is then removed from the platform [6]. The FDM process in detail is shown in Figure 2.

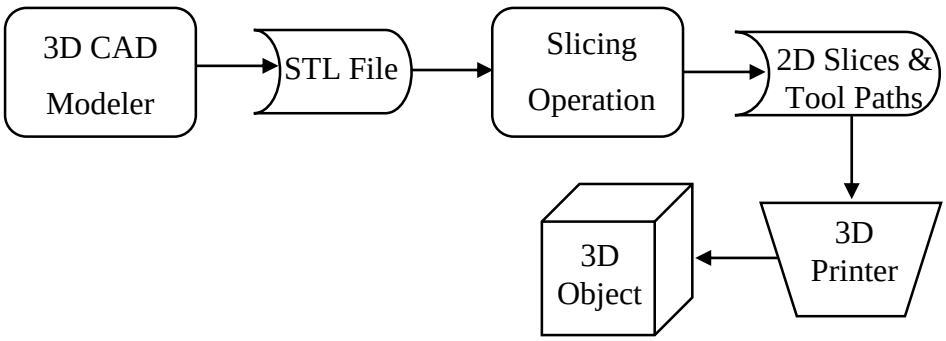

Figure 1. Steps of FDM process

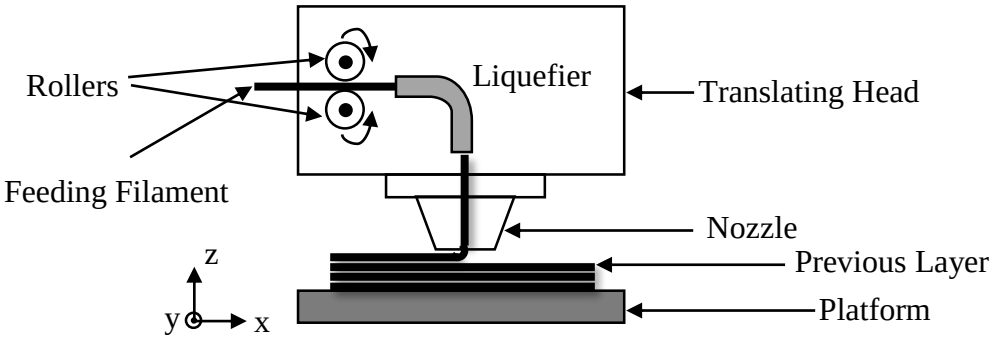

Figure 2. FDM process in detail

In FDM, there are different printing parameters and they have a great effect on the strength of the final object. Some of these parameters are filament width, raster to raster air gap and raster angle and they are shown in Figure 3. Also, the position of the successive layers with respect to each other is another printing parameter and it is called as raster orientation. Four most commonly used raster orientations are presented in Figure 4. From the aforementioned parameters, only filament width depends on the nozzle diameter and cannot be changed; whereas the others can be adjusted before the printing process.

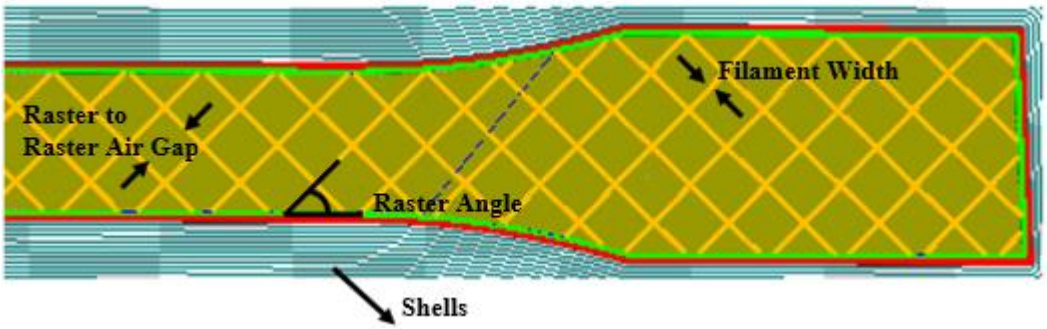

Figure 3. Printing parameters

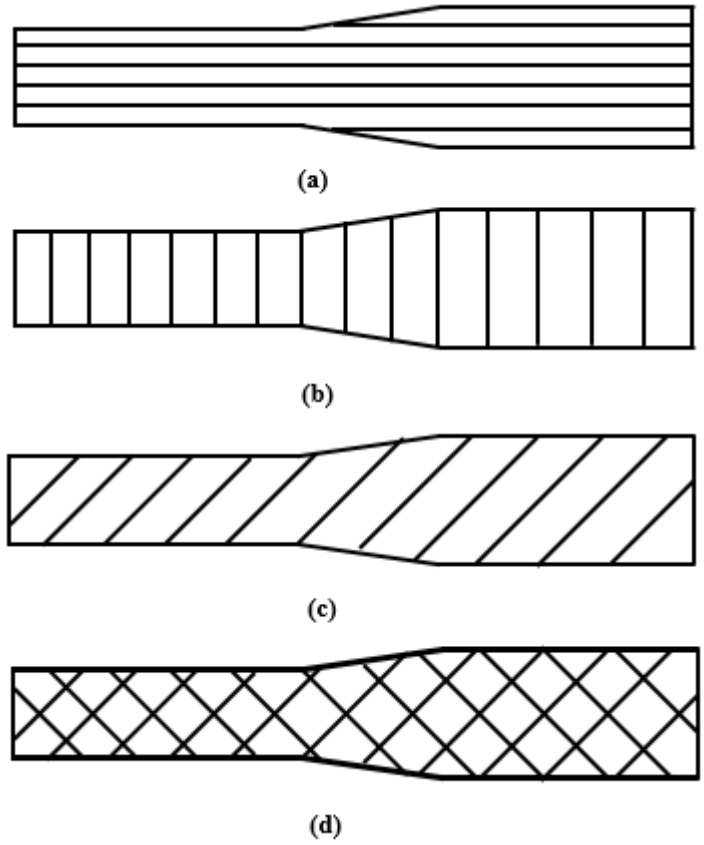

Figure 4. Raster orientations: (a) Longitudinal (0°), (b) Transverse (90 °), (c) Diagonal (45°), (d) Criss cross (default) (+45/-45°)

It is well known that FDM technology gained popularity after 2007, when Adrian Bowyer introduced an FDM-based printer which is capable of printing most of the parts that it is made of. As a result of this, RepRap project started. The aim of this project was to release the self-replicating 3D printer with open source license through-out the world [1]. This project had great success and from 2008 to 2011 the prices for 3D printers fell by 90 percent. As a result of cheaper 3D printer prices, the era of home use of 3D printers began [7].

Home fabrication is the last step of adoption of 3D printing. By home fabrication it is meant that end-users manufacture objects by using home-use 3D printers in their houses. However, there are not many people having 3D printers in their houses and those who do are mostly the hobbyist and students of engineering. The number of

people buying a “personal 3D printer”, which is a term used for printers which cost less than $5000, is increasing each year. Yet, when compared to the other electronic devices, sales are very low [8].

1.1. Motivation

It is well known that the usage of FDM expands in some industrial sectors like automotive, aerospace and medicine day by day [9]. On the other hand, home use of 3D printers is not at the expected level. This situation results from one specific limitation of personal 3D printers, which is the size of the printers. There is not enough printing volume in personal printers to produce useful parts. Only little toys, bibelots or tools can be printed. On the other hand, larger objects can be produced by partitioning them into smaller sub-parts that can fit into the printer. After printing the small parts, they can be glued together and the desired large object can be obtained.

The motivation of this study is to show that, the strength of the 3D printed objects can be truly determined by using numerical analyses without the necessity of any mechanical test. Doing tests in laboratories in order to determine the material properties is not always possible. Therefore, it is important to show that the similar strength values of an object can be determined by doing proper modelling of the object in a frequently used Finite Element Analysis (FEA) software like ANSYS.

Another objective of this study is to demonstrate that an object would have a similar strength, even though it cannot be printed as a whole, due to the limitation in the building volume of a 3D printer, but rather printed as sub-parts and bonded together by using a commercial adhesive. A case study is done with a helmet to show that the performance of the whole helmet and partitioned helmet are similar.

The current study also aims to fill some gaps in the literature. Although PLA is one of the most commonly used materials for FDM, there are not many studies which investigate the mechanical properties of it. That is why compression and tensile tests are done by using 3D printed PLA specimens.

1.2. Literature Review

The amount of published work about FDM is appreciable. The focus of many of the studies is on understanding the mechanical characteristics of the materials that are used in FDM [10,11]. In most of the studies, the mechanical properties of ABS material were investigated. Rodriguez [10] conducted some experiments to examine the mechanical properties of fused deposited (FD) ABS. He investigated the effect of manufacturing factors such as raster-to-raster gap, extrusion and envelope temperatures and extrusion deposition rate on two mesostructural variables; namely, void density and bond length density between adjacent filaments. He concluded that, the most important parameters are extrusion flow rate and raster-to-raster gap, whereas the temperatures do not have a significant effect on the mesostructural variables. Moreover, in order to observe the relationship between the material mesostructure and material properties, he did some experiments. He found out that after deposition the strength of the ABS filament decreases by 15% and the stiffness of the ABS filament reduces by 5%. He modeled the mesostructures analytically and numerically and showed that they are in good agreement with experimental results. Ziemian et al. [12] investigated the effect of raster orientation on the mechanical characteristics of ABS under tensile and fatigue loading. They manufactured four different types of specimens by using four different raster orientations, which are; longitudinal, diagonal, transverse, and the +45/-45 orientation: as the default raster of the machine. To obtain the reference values for tensile strength and mechanical behavior of ABS, they also manufactured specimens by using injection molding. As a result of tension tests, they concluded that the longitudinal raster orientation gives the highest tensile strength; however, it is lower than the reference value, which shows that layer by layer manufacturing affects the tensile strength of the material in a negative way. To identify the fatigue behavior of ABS specimens for different raster orientations, Ziemian et al. made tension-tension fatigue tests. The result of these tests revealed that the specimen deposited by using the default raster orientation had the longest fatigue life. On the other hand, the specimen which produced by using injection molding had a longer fatigue life. Mohamed et al. [9] experimentally investigated the time-dependent mechanical characteristics of FD polycarbonate (PC) ABS. They examined the effect of some printing

parameters such as slice thickness, raster-raster air gap, raster fill angle, the direction of deposition, filament width and the number of shells on creep displacement by applying definitive screening design. They found that increase in filament width and number of shells reduces the creep displacement. According to them, other methods that can be used to decrease the creep displacement are reducing layer thickness, air gap and raster fill angle. Cantrell et al. investigated the anisotropic behavior of PC and ABS material under tensile and shear loading [13]. They investigated the effect of raster and building orientation on mechanical properties of these materials. They also calculated the Poissons's ratio and strain energy density for both materials. In order to measure the average shear strain in the test section, they used Digital Image Correlation (DIC) technique instead of using strain gages. They concluded that ABS material showed isotropic behavior in terms of Young's modulus and Poisson's ratios for different orientations; however, anisotropy was found when ultimate strength, strain at failure and strain energy density values were compared. Moreover, they observed that raster orientation did not affect the tensile and shear properties of ABS; whereas, build orientation had great influence on them.

The number of studies investigating the mechanical properties of PLA is very limited. Casavola et al. [11] used ABS and PLA as printing materials to produce the specimens and did tensile tests with them in order to find their Young's modulus in transverse and longitudinal directions and to characterize the mechanical behavior of them by using classical laminate theory (CLT). They also compared the results for different raster angles. According to them, in FDM printers, mainly, thermoplastics like PLA and ABS were used in the past. They suggested that PLA has better thermo-mechanical properties compared to ABS, while it has larger mechanical resistance and smaller thermal expansion coefficient. The latter is important in printing since it reduces the effect of warping during the printing process. Song et al. [14] performed tension, compression and fracture experiments on 3D printed PLA material and investigated the response of the part along different directions. They observed highly anisotropic response with direction-dependent fracture behavior. On the other hand, they concluded that elastic response in transverse direction is isotropic; whereas, the inelastic re-

sponse is ductile and orthotropic. Letcher et al. [15] conducted tensile, bending, flexural and fatigue tests on 3D printed PLA specimens for three different raster orientations, which are 0° (longitudinal), 45° (diagonal) and 90° (transverse) directions. They also did the tensile test by using the PLA filament itself. They found out that strongest raster orientation for tensile loading is 45°. Moreover, the part having the same orientation had the highest endurance limit even though it has the similar fatigue life with 0° orientation. Chacon et al. [16] did a detailed investigation to characterize the effect of feed rate to liquefier, layer thickness and build orientation on mechanical properties of PLA parts. They found out that these process parameters have great influence on both strength and the stiffness of the material. They concluded that upright samples are the least strong and stiff ones: whereas flat and on-edge samples showed higher strength. In terms of layer thickness, they observed that for tensile and flexural tests the strength of the parts increased with increasing layer thickness; however, the ductile property decreased. Finally increasing feed rate caused a decrease in tensile and flexural strength of the up-right samples. On the other hand, no significant effect of the feed rate was observed for the other two orientations.

For different applications, various types of materials are required. Therefore, some researchers have developed new materials that can be used in FDM and searched the mechanical properties of them. Agarwala et al. [17] worked on the fused deposition of ceramics and metals. They used a variety of ceramic and metal particles in the fabrication of the parts. The manufactured parts were used in many different structural, electroceramic and bioceramic applications. These new filaments were able to meet the flexibility, stiffness and viscosity requirement of a successful FDM process. Gray et al. [18] developed a new high-performance thermoplastic composite for FDM, using thermotropic liquid crystalline polymer (TLCP). This material has a tensile modulus nearly four times as ABS. Nikzad et al. [19] examined the thermo-mechanical properties of ABS filled with the metal particle. They developed new filaments that can be successfully used in FDM by filling ABS with iron and copper particles separately. The new filaments showed higher stiffness than the pure ABS. In addition to that, the researchers concluded that the new filaments demonstrated promising results for future applications, in terms of thermal conductivity and dynamic mechanical

behavior. Similarly, Weng et al. [20] examined the thermal and mechanical behavior of the ABS/montmorillonite nanocomposites. They found that both tensile strength and thermal characteristics of ABS material are improved with the introduction of montmorillonite nanocomposites.

Considerably less research effort was devoted to the stresses and strains built up in 3D printed objects during the printing process. Lu et al. [21] investigated the strength to weight optimization of the 3D printed parts. They developed a hollowing optimization algorithm depending on the honey-comb cell structure. They hollowed the interior structure of the objects partially by considering the stress distribution in them. As a result, they were able to obtain even stronger parts. To verify their analysis, they printed the partially hollowed objects and measured their stresses and weights. Kantaros et al. [22] investigated the residual strains developed due to solidification by taking into two important parameters account, which are layer thickness and deposition orientation. By using an optical sensor with a short fiber Bragg grating (FBG) inserted at the mid-plane of 3D printed prismatic specimens, they recorded the developed residual strains. They produced 6 different specimens by using FDM. Half of them had a layer thickness of 0.25 mm and the other half had 0.5 mm. They used different raster orientations while producing each specimen; which were longitudinal (0°), transverse (90°) and default (+45°/-45°). They concluded that for thinner layer thickness, the developed residual strains were notably lower. When they compared different orientations, they observed that the residual strains were the lowest for transverse orientation which was nearly half of the strain values of longitudinal and default orientations. When they investigated the shrinkage induced residual strains, they concluded that the greatest strains are observed in the specimen which has 0.5 mm layer thickness with longitudinal raster orientation. Casavola et al. [23] measured the residual stresses in an FD ABS part by using the hole drilling method. In this method, a hole is introduced into a stressed body and this results in a regional stress relaxation and a deformation about the hole. An optical technique called electronic speckle pattern interferometry (ESPI) was used in this study to measure the stresses developed. The results were compared for different layer deposition angles. They found that the

worst stacking orientation is $\pm 30^{o}$ while it resulted in the highest residual stresses, and the best configuration is $\pm 45^{o}$.

There are not many studies about the partitioning of 3D printed objects. Lou et al. [24] applied partitioning to larger scale objects to make them suitable for the working volume of the 3D printer. They considered a number of criteria while partitioning, which are; assemblability, the minimum number of components, unnoticed juncture and structural strength. They developed a framework called Chopper, which optimizes these criteria and partitions the object either automatically or under a user guidance. In Chopper, the cut between any two parts is restricted by planar cuts which yield a Binary Space Partitioning (BSP) tree. They suggested that using this approach and giving up the convenience of arbitrary cuts results in an increased efficiency. Moreover, by using BSP, the optimization for printability and assemblability is naturally handled. Similarly, Hao et al. [25] stated that the easiest method for partitioning is planar division, which cuts the model into predetermined sized sub-parts by using certain planes. They suggested that the positions for cutting are selected through experience and inconvenient cutting positions may lead to even more complicated structures which will eventually affect the quality of the final part and efficiency. Song et al. [26] created a voxelization-based approach to divide a given 3D model into parts which can fit in the printing volume of the printer. With the help of the developed approach, they could obtain repeatedly dissembled and reassembled object which consists of strongly connected parts. While generating interlocking parts, they followed four steps. Firstly, they took the voxels in the internal volume as inputs and used an algorithm which iteratively extracts puzzle pieces from it in order to build interlocking puzzles. Secondly, they added the boundary voxels to initial 3D parts to obtain the required 3D shape. Thirdly, for aesthetic purposes, they checked the location of the connections in order to avoid placing the cutting seams in apparent locations. Finally, to take into consideration of the 3D printing machine tolerance, they created empty spacing by making the voxels on each side thinner. They concluded that interlocking 3D printed parts can be created by using the algorithm they developed. Mirkhalaf et al. [27] developed a bistable suture that can be cycled between two equilibrium states indefinite number of times. They tested this interlocked suture by 3D printing ABS

samples with different interlocking angles. They observed that when compared to plain ABS, the interlocked parts showed an improvement in toughness and strain at failure.

Photostress or photoelastic method is one of the three experimental methods that is used to observe the stress distribution on a part under loading. It provides full-field experiment and it is more successful than strain gauges while many of the limitations of strain gauges do not exist in photo-elastic method [28]. Before finite element analysis software was developed and improved so much, this method was used to observe the critical locations on an object. For many different purposes and in many different areas from dentistry to manufacture this method was used. Judge et al. [29] investigated the surface strain occurred on a dog scull under loading. To do that they coated the scull with an epoxy coating and they observed the strain distribution on the face when loaded under maximum of 1500N. They concluded that this method is useful and can be used to model the stress distribution on a human skull, which is loaded in vitro. Jankowski et al. [30] did 4-point bending test on carbon fiber reinforced plastic (CFRP) reinforced wooden beams and compared the results that they obtained by using strain gauges and photoelastic coating technique. They found out that two methods gave significantly different results due to different characteristics of wood in different locations. As another different application, Cevik investigated the stress generated in fillet welds by using the photoelasticity method in his thesis [31]. He concluded that this method is very useful to determine the stress distribution on machine elements, while it causes no damage on the tested material. He also compared the results with theoretically calculated results and concluded that they were very close to each other. Another conclusion he made was this method is not very appropriate to observe the stress distribution on the small surfaces.

1.3. Contribution of the Thesis

Even though PLA is one of the most frequently used material in FDM, there are not many studies about its mechanical properties. There are some investigations focusing on some of the mechanical properties of the 3D printed PLA material; however, there

are not many studies about its properties under compression loading. Indeed, as far as the author's knowledge, there is no study which compares the effect of infill percentages on mechanical properties of 3D printed PLA under compression loading. The Young's modulus of 3D printed PLA is calculated under compression loading for 100% infill and 20% infill specimens. This thesis provides a complete study by investigating the properties of 3D printed PLA both experimentally and numerically.

In addition to that, this thesis uses photo-stress analysis on a 3D printed PLA material to observe the stress distribution. For the best of the author's knowledge, photo-stress technique has not been used on a 3D printed object before.

One of the important aspects of this study is to investigate the effect of partitioning and joining the parts, on the strength of the object. As a result of this study, it is shown that both objects show similar performances. However, one should note that the strength of the object highly depends on the partitioning regions and the strength of the adhesive.

Finally, in this study a motorcycle helmet is used as a case study. To simulate the impact on the helmet, results of one of the most detailed report, which was prepared about motorcycle accidents, is used. As far as the author's knowledge, this report has never been used for such a purpose.

1.4.Overview of the Thesis

The main objective of this thesis is to analyze the mechanical stresses occurred in a 3D printed part. To understand the mechanical property and the behavior of the 3D printed PLA, specimens were produced, compression and tensile tests were conducted. Afterwards, numerical analyses for these tests were done. In the final chapter, as a case study a helmet was modelled. The results for the whole helmet and partitioned and glued helmet are compared. The outline of the thesis is as follows.

In Chapter 2, the details of experimental setup and numerical analyses are presented. In the first section, the process of each test is explained in detail, and corresponding results are shown. In the second section, the numerical modelling for the tests are

explained and results are presented. Last section is dedicated to the comparison of experimental and numerical analyses results. The similarities and differences of the numerical analyses results and experimental results are discussed and possible sources of discrepancies are explained. Moreover, for both compression and tensile test specimens, the mechanical properties for different infill percentages are estimated by using the properties of the bulk specimens.

In Chapter 3, the case study is presented. At the beginning of this chapter, the object to be modeled for the case study is decided as a motorcycle helmet and the reasons behind choosing this object are explained. Then the numerical modeling of motorcycle helmet, is done. As the last section of this chapter, analyses are done to find the most critical impact direction, stress distribution on the adhesive region for critical regions and the results are presented. Also two different methods that can be used for partitioning the helmet is explained.

In Chapter 4, present study is summarized. Furthermore, the concluding remarks are presented. In the final section of this chapter, some suggestions are made for the future work that can extend this study.

CHAPTER 2

EXPERIMENTAL PROCEDURE AND NUMERICAL VERIFICATION

This chapter is divided into three main sections. In Section 2.1, the details about the compression, tensile and photostress tests are explained and corresponding results are presented. The results are then compared with the results of similar studies. In Section 2.2., numerical modelling process for each test is explained in detail and the results of numerical analyses are presented. In the last section of this chapter, the numerical analyses results are compared with the experimental results and discussion is made.

2.1. Experimental Setup and Procedure

2.1.1. Printing Conditions of the Specimens

The specimens for tensile and compression stress tests were produced by using Ultimaker 2 3D printer, which is shown in Figure 5. Specifications for Ultimaker 2 are tabulated in Table 1.

In Ultimaker 2, there are controllable parameters such as nozzle operation temperature, heated bed operation temperature and extrusion speed. These factors have significant effect on the final part quality. Moreover, for different filament materials, proper operating conditions should be adjusted. PLA filament was used in this study. PLA was chosen because when compared to ABS it has a lower melting point, which results in easier printing process. For that reason, PLA is commonly used in home-use 3D printers.

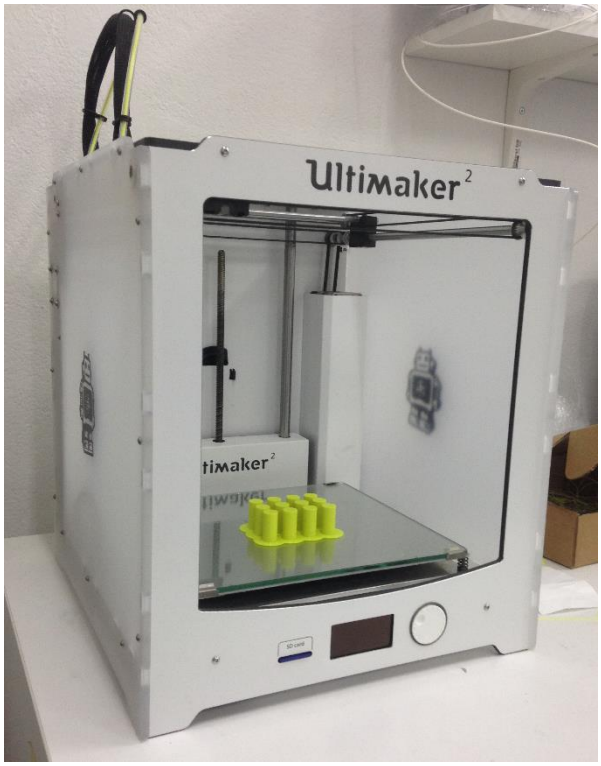

Figure 5. A photograph of Ultimaker 2 3D Printer

Table 1. Ultimaker 2 Specifications [35]

Property	**Value**
Build volume (mm^3)	223*223*205
Layer resolution (mm)	
Fast	0.2
Normal	0.1
High	0.06
Ulti	0.04
Filament diameter (mm)	2.85
Extrusion speed (mm/s)	60
Nozzle diameter (mm)	0.4

All of the specimens were produced from the same spool of PLA filament and the used filament was a product of ColorFabb having fluorescent green color. The specimens were produced with the operating conditions, given in Table 2.

Table 2. Operating Conditions

Property	**Value**
Nozzle operation temperature (ºC)	210
Heated bed operation temperature (ºC)	60
Environment temperature (ºC)	22
Extrusion speed (mm/s)	60

Thermal stresses occurred during the deposition of the object and they are highly depending on the operating temperatures tabulated in Table 2. However, the thermal stresses are out of scope of this study.

2.1.2. Compression Test

2.1.2.1. Compression Test Process

For the compression test, total of 12 specimens were produced. The compression test specimen has a diameter of 12.7 mm and a length of 25.4 mm which are the preferred dimensions for ASTM D695-15 standard [32]. A photograph of a produced part is presented in Figure 6. Even though all of the specimens were produced at the same time, under the same conditions, slight differences in the dimensions of different specimens were observed. These differences were in order of tenth of a millimeter.

In order to observe the effect of infill percentage of the produced part on the final object strength; half of the specimens were produced with 20% infill, which is the

default infill percentage for the Ultimaker 2 device, whereas the other half were produced with 100% infill. The default raster orientation (+45°/-45°) is used during the printing of the specimens. Build direction, interior infill pattern and raster angle are shown in Figure 7.

Figure 6. A photograph of compression test specimen

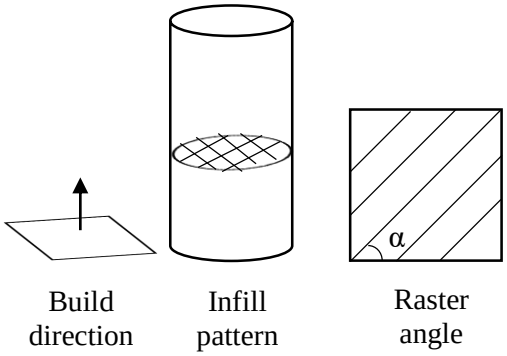

Figure 7. Specimen printing details

To conduct the compression tests Zwick/Roell Z020 machine was used. This machine has a maximum loading capacity of 20 kN. In the compression test, specimen was compressed between two square plates. Side dimension of each plate is 19.5 cm. Each plate consists of 9 smaller plates. The specimen was placed at the center of the square plate in the middle. This plate has an edge length of 54 mm. All of the specimens were

placed almost at the same location. A photograph showing the plates and the specimen is presented in Figure 8.

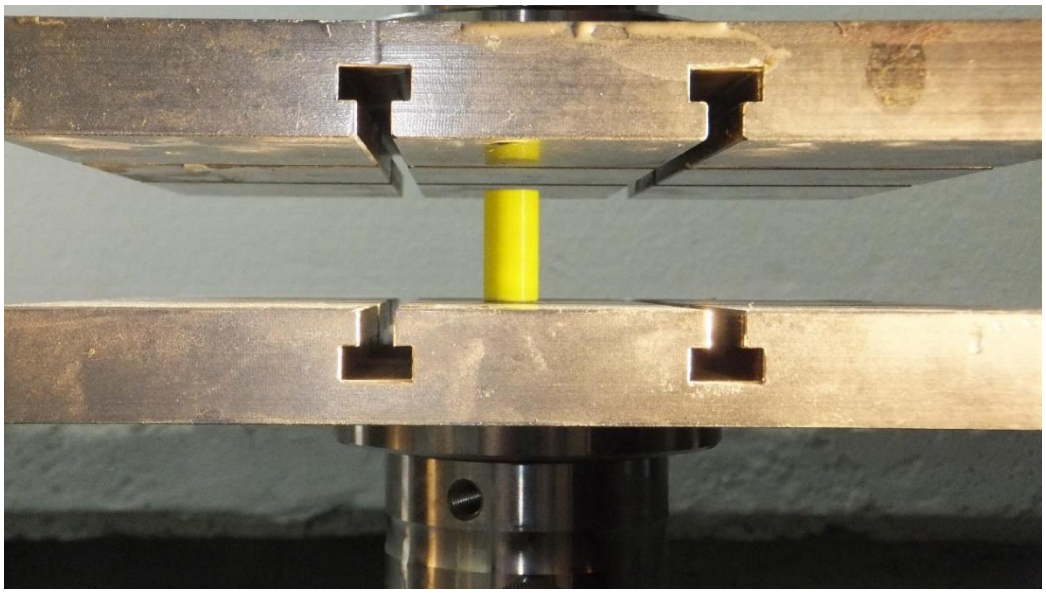

Figure 8. Compression test setup

Initial gap between the specimen and plate was set to 2 mm. Speed of the upper plate was set to 3 mm/min. The upper and lower faces of the specimens were greased in order to reduce the friction between the plates and the surfaces. The movement of the upper plate continued a while after the failure of the material occurred. After that, the machine is unloaded. All of the compression tests were done at room temperature, which was approximately 20°C. During the compression tests the force applied on the specimens were measured by load cells.

2.1.2.2. Compression Test Results

2.1.2.2.1. Specimen with 20 Percent Infill

Linear property of the material was checked first. In order to do that, specimen 1 was loaded to a certain force value in the elastic region, and then unloaded. The specimen showed almost linear behavior. The result is presented in Figure 9.

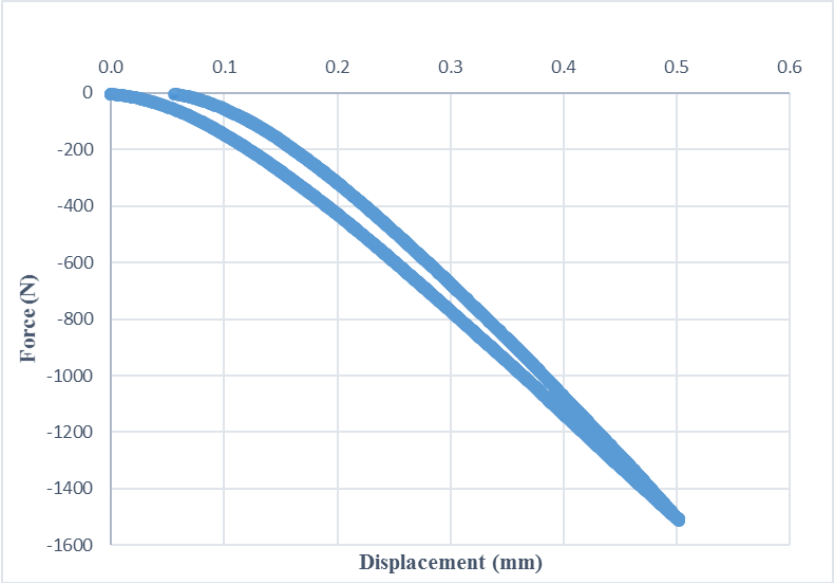

Figure 9. Force-displacement graph of 20% infill cylindrical specimen for loading and unloading in linear region

The compression tests were conducted for five specimens under the same conditions. Three of them failed by forming a swelling in the middle of the specimen. Two of them however, failed by forming a swelling or somehow melting near the bottom surface of the specimen. The pictures of specimens failed in different modes can be seen in Figure 10.

Figure 10. 20% infill cylindrical specimens failed from various regions

By using the data received from the load cell and the displacement value read from the computer during the tests, the force displacement graph for each specimen was drawn. Force displacement graph of all five specimens are plotted on the same figure and it is presented in Figure 11.

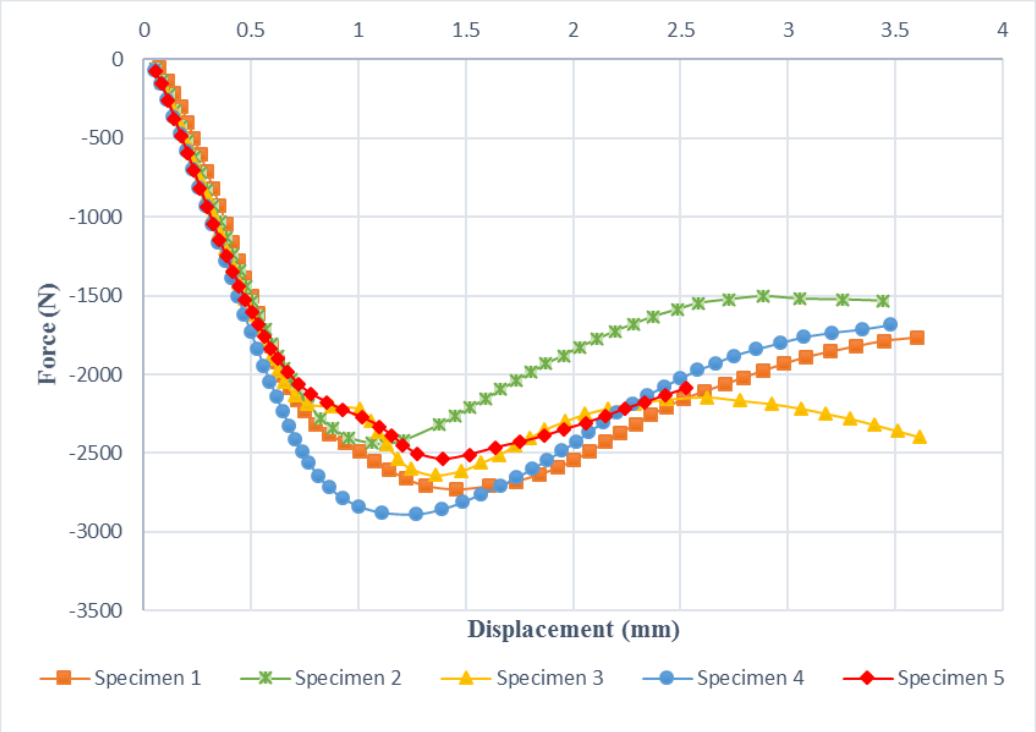

Figure 11. Force-displacement graph for 20% infill cylindrical specimens

From Figure 11, it can be interpreted that the force under which the specimens failed, has a range between around 2500 N and 2800 N. Except for the specimen 3 and 5, the force-displacement plots are similar.

From the force-displacement graph, stress-strain graph can be obtained by dividing the force by the initial cross sectional area, and the displacement by the initial length of the specimen. The stress strain graph for specimens 3 and 5 are presented in Figure 12, separately to make a more detailed investigation possible and from the figure, around strain value of 0.03, yielding of the specimens can be observed. This behavior

was only observed for these two specimens and it can be a result of failing from the bottom section.

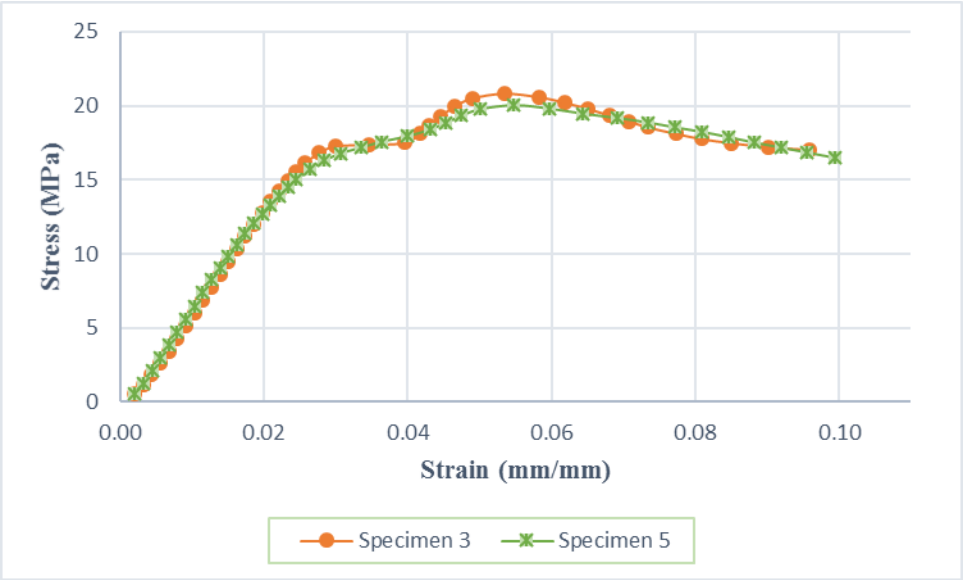

Figure 12. Stress-strain diagram of 20% infill cylindrical specimens 3 and 5

.

2.1.2.2.2. Specimen with 100 Percent Infill

As it was done for the 20% infill specimen, as a first step, the linear property of the specimen is checked by using the aforementioned procedure. The fully solid specimen also showed linear property in elastic region. The result can be seen in Figure 13. When compared with the 20% infill specimen, it showed more linear behavior. This may result from the more uniform infill properties of the 100% specimen.

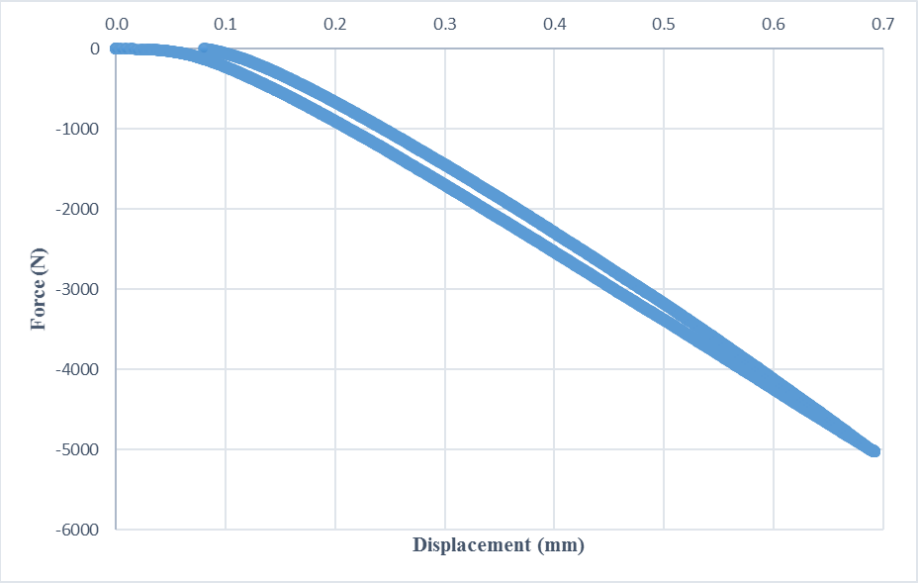

Figure 13. Force-displacement graph of 100% infill cylindrical specimen for loading and unloading in linear region

The compression tests were conducted for five specimens under the same conditions. All of them failed by forming a swelling in the near middle of the specimen. The place of the swelling region was closer to upper surface for four of the specimens and for one of them the region was closer to the lower surface. The picture showing the failed specimens can be seen in Figure 14.

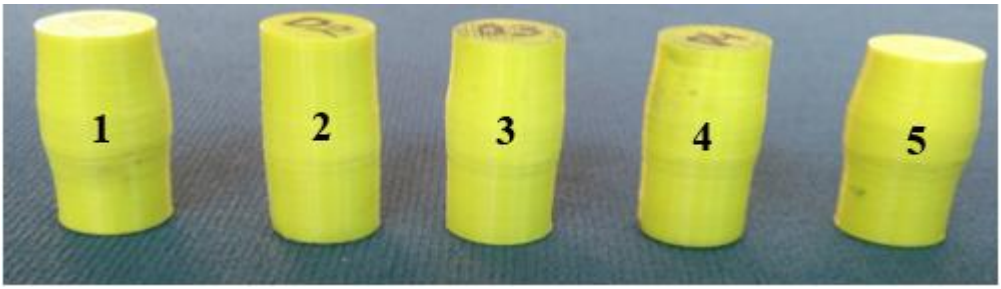

Figure 14. 100% infill cylindrical failed specimens

During the tests, the force data was collected from the load cell and force-displacement graph of all specimens were plotted. These plots were then collected on the same graph and it is illustrated in Figure 15.

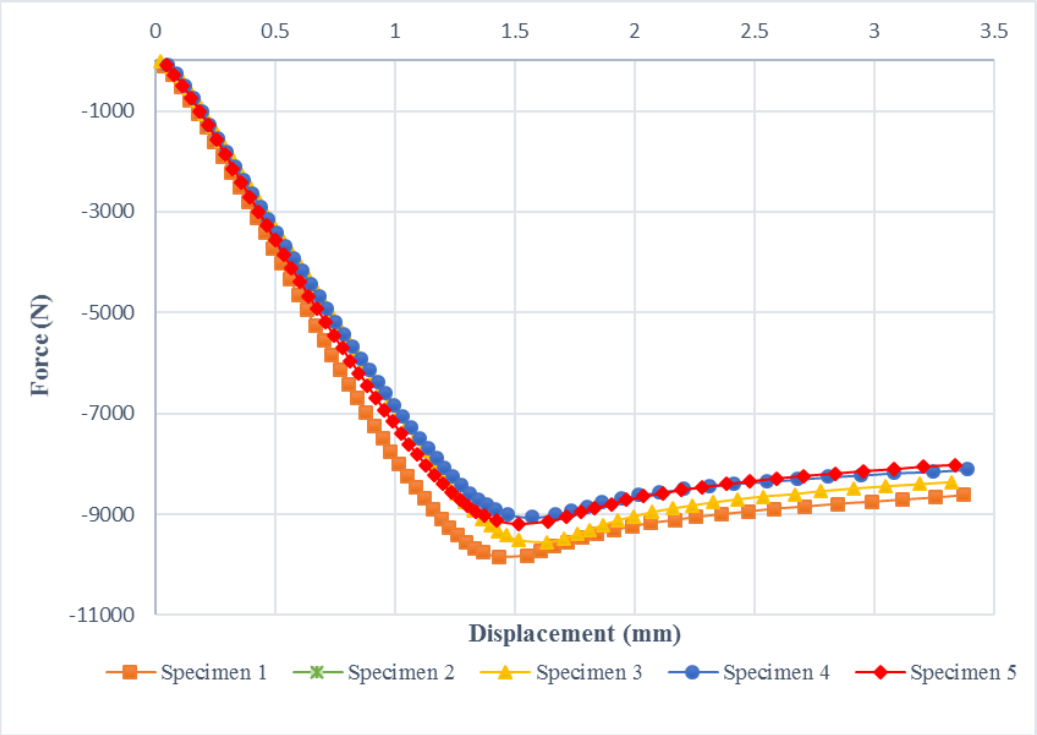

Figure 15. Force-displacement graph for 100%infill cylindrical specimens

From Figure 15, it can be clearly seen that the force under which the specimens failed changes between around 9000 N and 10000 N. For all the specimens, the force-displacement plots show similar behavior.

When the force displacement figures for different infill percentage specimens are compared, it can be seen that the behavior of fully solid specimens more alike to each other than that of 20% infill specimens. This may result from the uniformity of the interior part of the solid specimen. In 20% infill case, even a slight difference of interior structure would cause greater difference. This difference may be caused by the deposition sensitivity of the 3D printer.

Ultimate strength is the maximum value at which the specimen fails. Yield strength can be determined by drawing a parallel line to the original curve with 0.2% offset value [13]. The intersection of this straight line with the original curve gives the yield strength. Young's modulus of each specimen was calculated in the elastic region which is up to yield strength value. Hooke's law was used while calculating the Young's modulus and according to Hooke's law the ratio of stress over strain in elastic region is equal to the Young's modulus of the material. A summary of ultimate yield strength, yield strength and Young's modulus of each specimen are given in Table 3 and the average of these mechanical properties for all specimens are calculated.

When the results for 20% infill and fully solid specimens were compared, it can be concluded that fully solid specimens have greater strength, as expected. The average yield strength of 100% infill specimens is 70.71 MPa, which is almost 4 times greater than the yield strength of 20% infill specimens. It can be concluded that infill percentage increases the strength of the material; however, the relationship is not linear.

To understand the effect of infill percentage on strength explicitly, stress-strain plot of specimens having different infill percentages should be plotted on the same figure. As an example, from each infill percentage, the specimens having the greatest strength were chosen and plotted in Figure 16.

From Figure 16, it can be inferred that the behavior of both types of specimens are similar. For both of them, stress increases with strain linearly up to failure point.

Most of the studies done in the literature used the specimens made of ABS material. As far as the author's knowledge, up to now no study investigates the infill percentage on the final object's strength for the PLA filament under compression test. However, Song et al. did compression test on 100% infill cubic specimens and they investigated the effect of raster angle [14]. They also compared the mechanical properties of 3D printed PLA and the injection molded PLA. They found that for 1.25×10^{-5} strain rate, yield strength of 3D printed PLA was 78.19 MPa. In this study 1.95×10^{-5} strain rate was used and average yield strength of 100% infill specimens was found as 70.71 MPa, which is about 10% less. They also calculated the elastic modulus of PLA as

3.42 GPa. This value is more than twice the value that was found in this study. The source of deviation may result from the usage of different PLA material and the difference between the shape of used specimens.

Table 3. Compression test results for all specimens

Infill Percentage	**Specimen Number**	**Ultimate Strength(MPa)**	**Yield Strength(MPa)**	**Young's Modulus(MPa)**
20%	1	21.57	18.31	676.49
	2	19.27	17.35	650.12
	3	20.85	16.81	690.51
	4	22.82	20.85	712.19
	5	20.04	15.69	649.88
	Average	**21.13**	**17.80**	**675.84**
100%	1	77.84	73.12	1620.8
	2	78.89	74.65	1629.5
	3	75.49	71.73	1446.2
	4	71.53	67.73	1396.6
	5	72.55	66.3	1495.2
	Average	**75.26**	**70.71**	**1517.66**

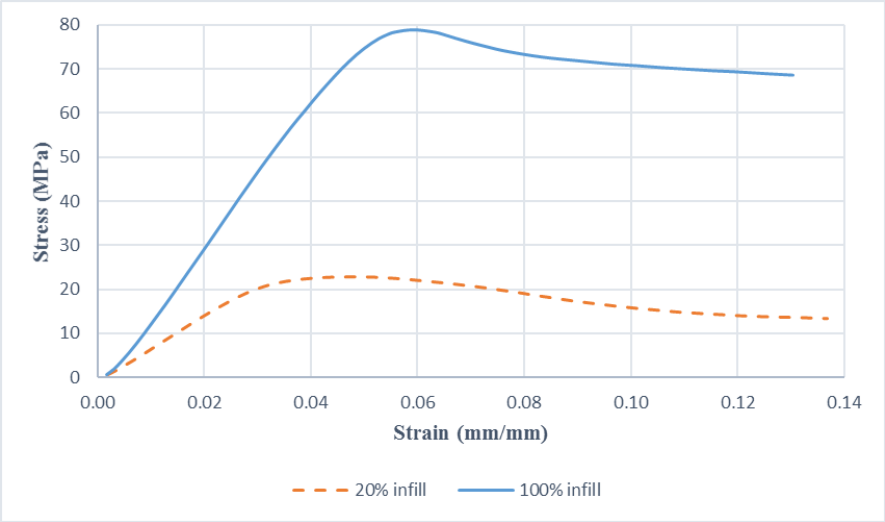

Figure 16. Stress-strain diagram of different infill percentage cylindrical specimen

Sood et al. [33] investigated the behavior of ABS P400 material under compression loading. They reported that at the beginning of compression test, stress changes with strain linearly. In this study, similar behavior was observed. They also noted that, after the initiation of the cracks, the behavior becomes non-linear and in nonlinear region stair step formation occurred up to fracture, indicating that material continues to deform [33]. This type of behavior wasn't observed for any of the 100% infill PLA specimens. However, it was observed for two of the specimens having 20% infill (Specimens 3&5). Moreover, none of the specimens fractured on the contrary to ABS P400 specimens.

Inspection of the failed specimens showed that specimens did not break into multiple pieces, but they remained as one piece. Ziemian et. al [34], did compression test with similarly shaped specimens by using ABS filament in printing. They found out that specimens failed by separating into two or three pieces. This failing mode was not observed for the PLA specimens. In addition, they reported that for same raster orientation yield strength of ABS specimen was 28.14 MPa [34]. The average yield strength for PLA is 70.71, which is much greater than the ABS.

2.1.3. Tensile Test

2.1.3.1. Tensile Test Process

For the tensile tests, total of 5 specimens were produced. The shapes of the specimens complied with the ASTM D638 standard [35]. In Figure 17, a photograph of tensile test specimen is presented. This type of tensile test specimen is also called as flat dog bone specimen. For tensile test, all of the specimens were printed with infill percentage of 20%. Raster angle and infill pattern was chosen same as compression test specimen. The specimens were printed upon their largest surface. Although all of the specimens were produced at the same time and under the same conditions, slight differences in the dimensions of different specimens were observed. Moreover within the same specimen, the width and thickness values were measured to be different, even though in the regions they should be the same. These differences were on the order of hundred micrometer and could be caused by the sensitivity of the used 3D printer.

Figure 17. A photograph of tensile test (flat dog bone) specimen

In order to measure the strength of the adhesive, two couples of half tensile specimens were produced. A picture of half specimen and glued halves are shown in Figure 18.

The first group of half specimens were glued by using 502 Cyanoarylate Adhesive Evobond (from now on it will be referred as 502CAE), which is a commercial adhesive that can be found in the market easily. Immediately after applying this adhesive to the desired surface, the catalyst was sprayed and solidification of the adhesive was obtained instantly. The glued specimen was then cured for 24 hours. To bond the sec-

ond group of specimens, Tangit Hard PVC Adhesive was used. Tangit is also a commercial adhesive and can be obtained easily from the market. The waiting period for it was also 24 hours.

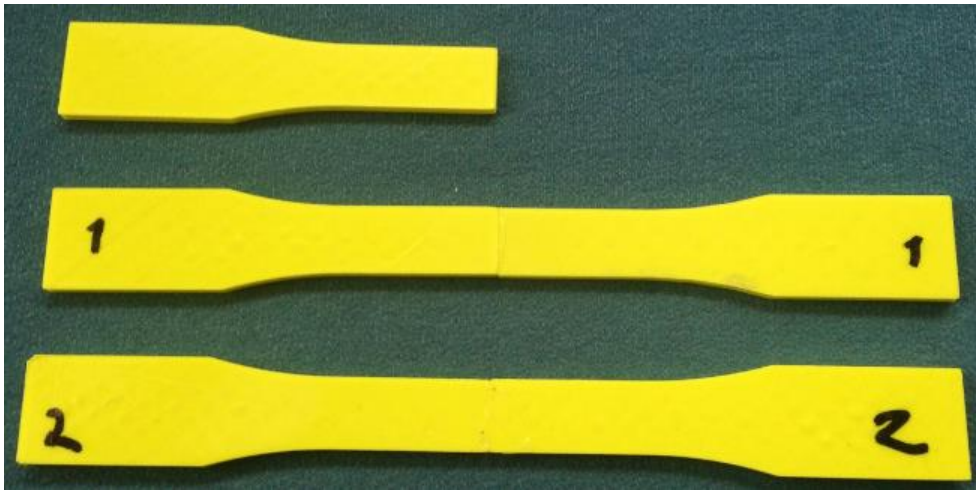

Figure 18. A picture of half specimen and two halves glued together

As an unsuccessful trial, the specimens were bonded by using Pattex two-component adhesive. The solidification time of this adhesive was very long when compare to the first adhesive. Also, even after 24 hours curing time exceeded, the bond between the specimens couldn't be reached. It can be concluded that, even though Pattex is a very strong commercial adhesive, it is not suitable to use with PLA material.

Zwick/Roell Z020 machine was used for the tensile tests as well. The specimens were gripped from two ends. While placing the specimens within the grippers, the important aspect is that the grippers hold the specimens from the thicker section in order to prevent failure from the deformation created by the grippers. Rather than that, the place of holding is not very important as long as it is in the thicker region. A photograph of the experimental set-up is shown in Figure 19. To get more detailed information about the deformation in gage length region of the specimen, an extensometer was connected to specimen 5. It measured and recorded the displacement specifically in this region. A picture of the specimen with extensometer can be seen in Figure 20.

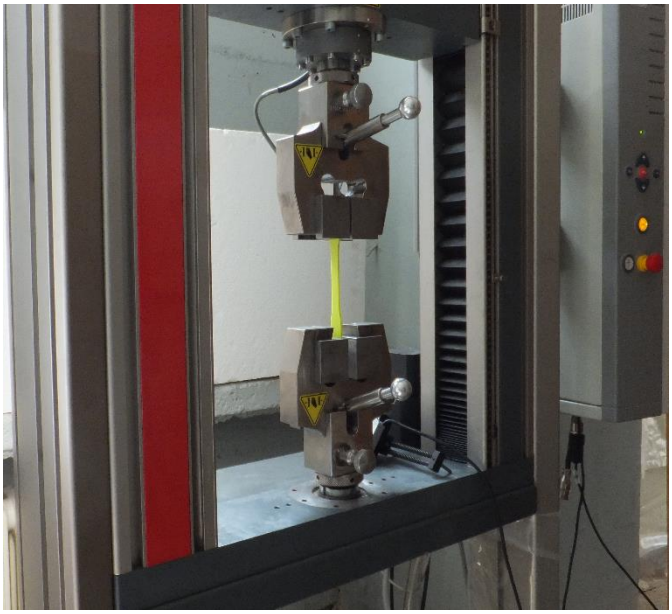

Figure 19. Tensile test set up

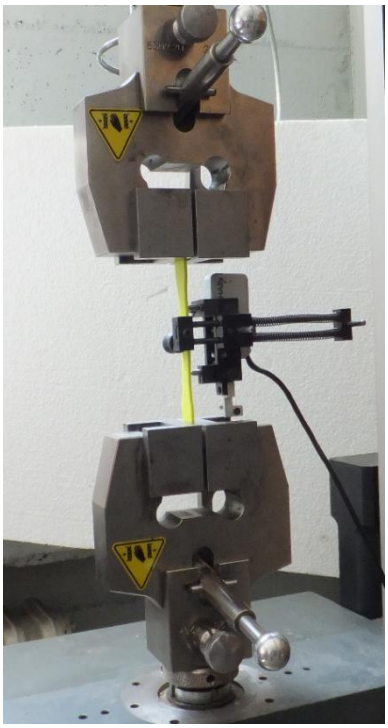

Figure 20. Tensile test specimen with extensometer

Speed of the upper plate was set to 3 mm/min. The machine was stopped right after the fracture of the material. In addition to that, all of the tensile tests were done at

room temperature, which was approximately 20°C. During the tensile tests the force applied on the specimens were measured by load cells.

2.1.3.2. Tensile Test Results

In tensile test, the specimens failed from the weakest region. As noted before, prior to the tests, when the dimensions were measured, slight differences within each specimen dimensions and between different specimens were observed. These variations caused the specimens to fail at different locations. On the other hand, all of the specimens showed a common behavior as well. No necking was observed and the specimens failed before elongating too much. The failing region for each specimen can be seen in Figure 21. Using the data that was recorded by the load cell during the experiment, force-displacement results were plotted for each specimen. These results were combined on the same graph and are shown in Figure 22.

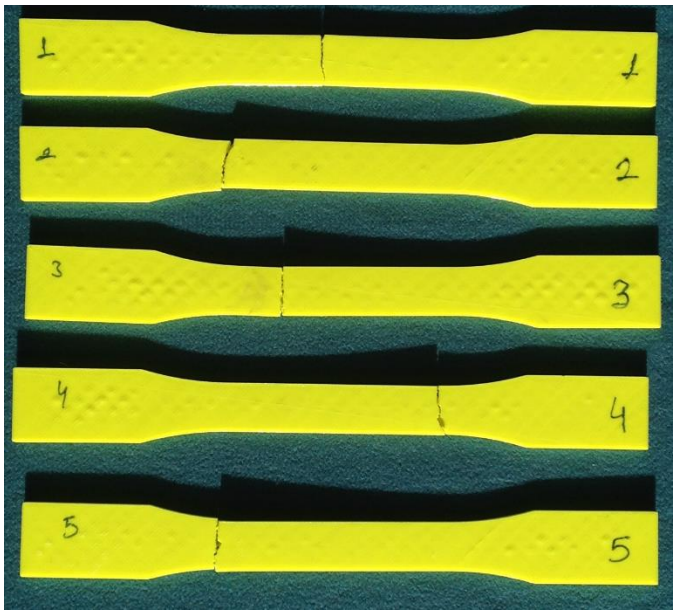

Figure 21. Failing region of flat dog bone specimens

As it can be seen in Figure 22, the trend of the curves are similar for all of the specimens. The maximum force before failure changes between 730 and 800 N.

From force-displacement data, stress strain values can be obtained. Engineering stress equals to force divided by initial cross sectional area and engineering strain equals to ratio of displacement to gage length. Engineering stress-strain diagram for all of the specimens are shown in Figure 23.

By examining Figure 23, some conclusions about the 3D printed PLA object under tensile loading can be made. First, the parts did not show yielding prior to failure, but rather they fractured suddenly. Second, the slopes of the curves are not very sharp. In other words, the material showed a brittle plastic behavior. To make it more clear, the mechanical properties found by using Figure 23 are tabulated in Table 4.

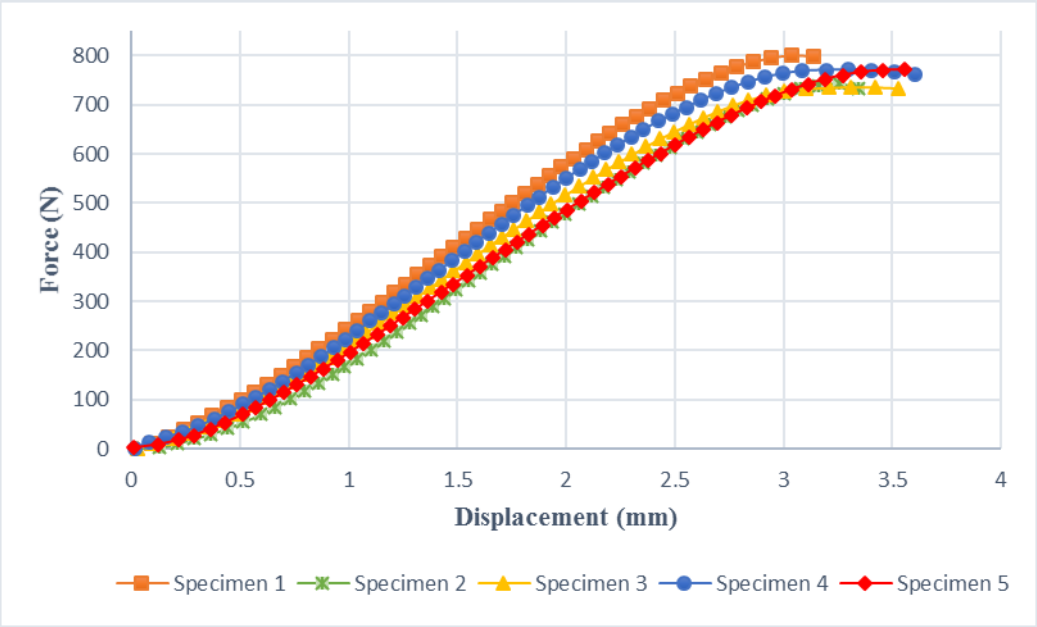

Figure 22. Force-displacement graph of all flat dog bone specimens

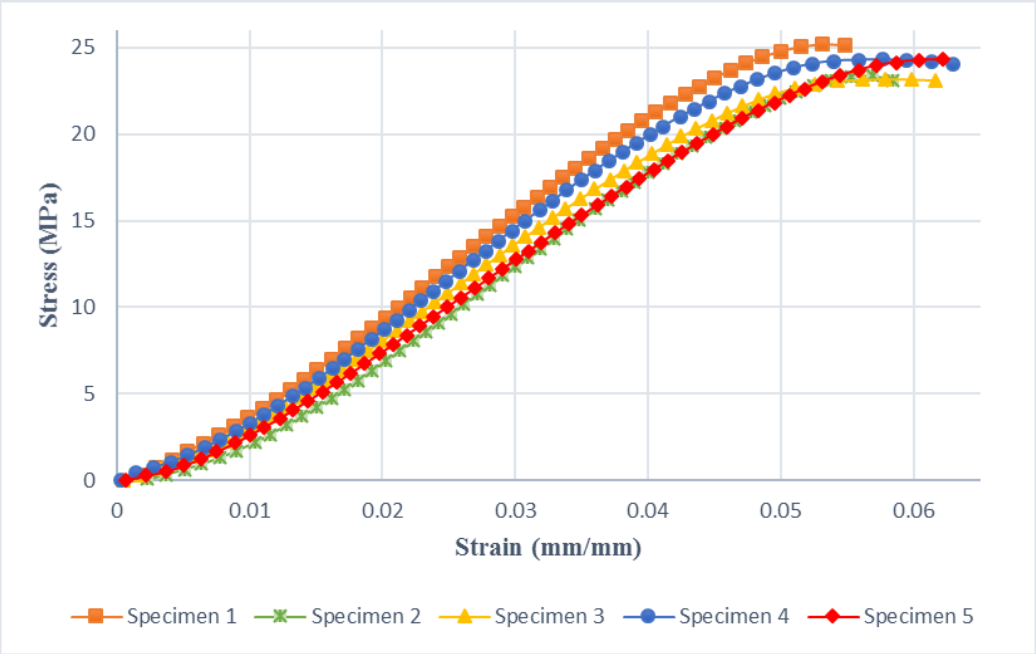

Figure 23. True stress-strain graph of all flat dog bone specimens

Table 4. Tensile test results for all specimens

Infill Percentage	Specimen Number	Ultimate Strength(MPa)	Yield Strength(MPa)	Young's Modulus(MPa)
20%	1	25.2	24.47	559.7
	2	23.37	22.44	584.3
	3	23.19	22.34	502.1
	4	24.28	22.75	554.3
	5	24.29	23.02	484.2
	Average	**24.07**	**23.00**	**536.92**

By investigating Table 4, it can be said that yield strength is close to ultimate tensile strength. Moreover, on the contrary to most metals, fracture occurs at the maximum stress. The results showed that among the five specimens, maximum yield strength is

24.47 MPa, whereas the minimum yield strength is 22.34 MPa. The average yield strength of the five specimens is 23 MPa. The maximum yield strength deviates from the average by 6.4%; while deviation of minimum yield strength is 2.9%. When the Young's modulus results are investigated, the average value is calculated as 536.92 MPa. The deviation of this value from the maximum value is 8.8%; whereas it is 9.8% from the minimum value.

It would be better to use an extensometer in order to record the displacement occurred in the region of interest. However, in this study it was observed that when the extensometer was attached to the specimen, which was specimen 5, it caused a bending. Therefore, for the other specimens extensometer was not used. This may have caused some error in strain calculations.

When the results were examined, the Young's modulus for the specimen with extensometer was observed to be about 10% smaller than the average value. Even though this was not a great difference, it would be caused by the extensometer.

Furthermore, the average Young's Modulus result found for the tensile test was lower than the average result of compression test done with the same infill percentage specimens, by 25%. Another words, PLA has tension/compression asymmetry. Song et al. also reached this conclusion in their study [14]. In general, materials show symmetric behavior in elastic region, which means they have the same Young's modulus under tension and compression loading. Yet, PLA shows an asymmetric behavior.

In their study, Song et al investigated the effect of raster angle on tensile strength of 3D printed PLA [14]. For 100% infill specimen printed with 45°raster angle, they found the tensile strength to be around 95 MPa. The infill percentage used in this study was 20% and the corresponding tensile strength was 23 MPa. It can be concluded that, infill percentage has a large effect on tensile strength of 3D printed PLA.

Wu et al. [36] did tensile tests with ABS and polyether-ether-kethone (PEEK) specimens and they reported the pictures of failed specimens. Similar to this study, all of the specimens failed at different points.

Hwang et al [4] examined the effect of infill percentage on tensile strength of ABS material and they found out that tensile strength increases with infill density, as expected. According to their results, tensile strength of 20% infill specimen is 26 MPa, whereas it was found as 24 MPa in this study for PLA. Moreover, the stress-strain diagram of ABS material showed that ABS material fails after the maximum stress point exceeded regardless of the infill density [4]. On the other hand, PLA specimens failed at the maximum stress value.

After obtaining the mechanical properties of PLA by using whole tensile test specimens, the behavior of half specimens was investigated which were bonded by using different adhesives When tensile test was done with the glued specimens, it was observed that both of the them failed from the adhesive layer region. This proves that when two parts were glued together, the strength of the part is determined by the strength of the adhesive. For two different adhesives the force-displacement curves are shown in Figure 24.

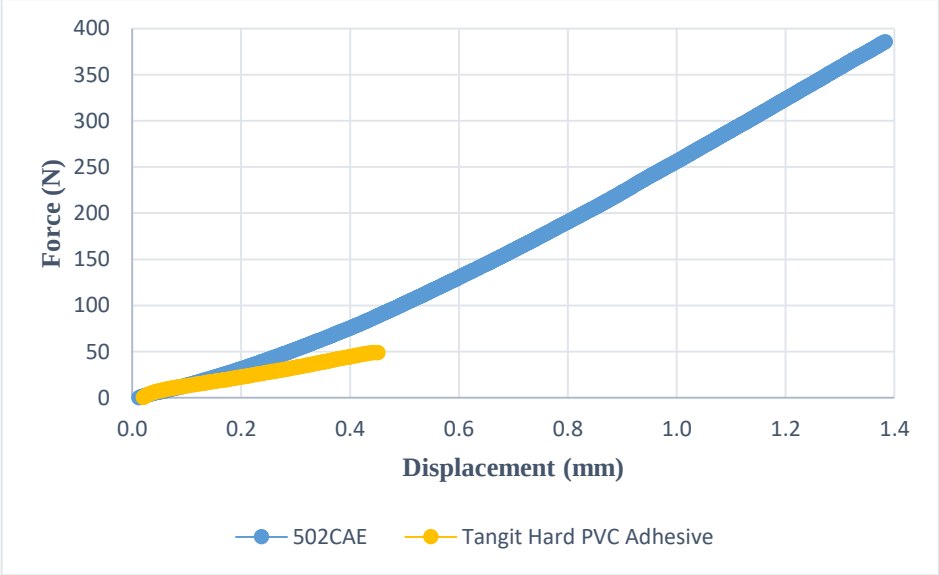

Figure 24. Force-displacement graph for two different adhesives

From Figure 24, it can be clearly seen that 502CAE is stronger than Tangit hard PVC adhesive. The maximum force which 502CAE can withstand was almost 8 times of Tangit hard PVC adhesive. In consequence, 502CAE was decided to use in the numerical analyses part. The results obtained from the experiment is tabulated in Table 5.

Table 5. Properties of 502CAE

Property	**Value**
Young's Modulus (MPa)	519.44
Yield Strength (MPa)	12.12

2.1.4. Photostress Test

2.1.4.1. Photostress Test Process

A reflection polariscope is required in order to conduct the photostress analysis. In this study PhotoStress Plus LF/Z-2 Reflection polariscope was used.

In photostress test the material should reflect the light or should be coated with a material that reflects the light. After that the test material should be coated with a special semitransparent material which has birefringent property. The working principal of the reflection polariscope is schematically represented in Figure 25.

The specimen is ready for the photostress analysis once the coating is done. As soon as the loading starts on the test part, the coating is illuminated by the polarized light that is coming from a reflection polariscope. Under loading, when it is looked through the polariscope, the coating shows the strains in a colorful way; and thus reveals the most critical regions that have higher strains [37]. The color schematic can be seen in Figure 26.

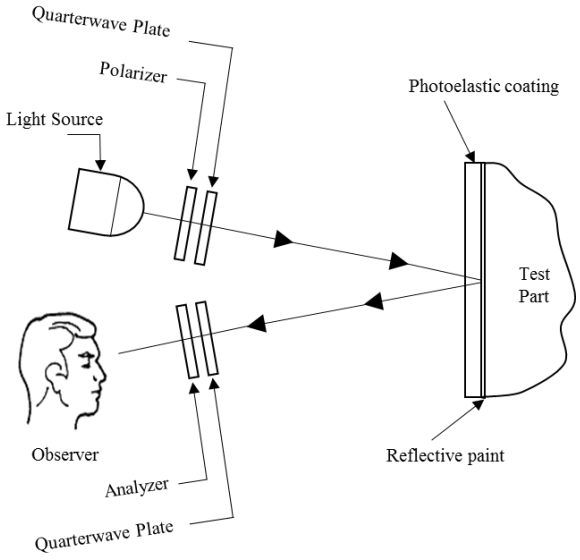

Figure 25. Represantation of reflective polariscope

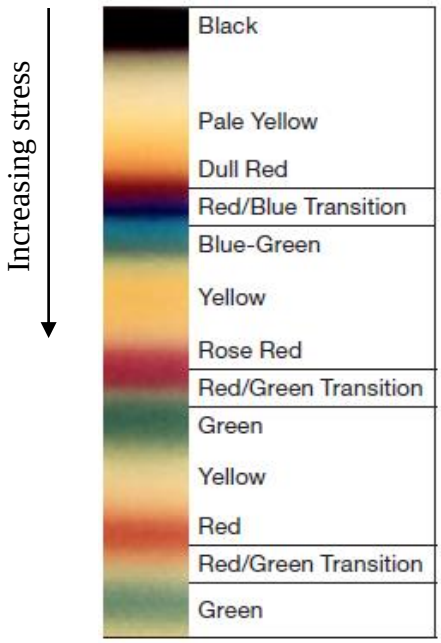

Figure 26. The color schematic with increasing stress [37]

In this study, photostress analysis was done with specimens made of PLA. The photostress tests were conducted for a 100% infill compression specimen and a tensile test specimen. Since PLA is not a reflective material, the specimens were coated with a silver paint, first. After this thin layer of reflective paint dried completely, the specimens were coated with Epoxy resin, which has quite good birefringent property. Epoxy resin consists of two components and the mixing ratio of them is 1:2. For both paint layer and epoxy layer, the required time of drying was approximately one day. When the two components of the epoxy resin were mixed, the obtained mixture is in liquid form and it is not easy to obtain a coating which has a uniform thickness. In order to achieve this uniform coating layer, tensile test specimens were produced with 1 mm frame around them, and epoxy resin was poured on it. Afterwards, the frame was broken and tensile test specimen with uniform coating was obtained. For the compression test specimens, a special mold was created such that half of the specimen could be coated with a uniform thickness resin. After this mold was filled with epoxy resin, the specimen was placed in the mold at certain height. As a result, uniform coating thickness was obtained on the half surface of the specimen. The pictures of coated tensile test specimens are shown in Figure 27 and coated compression test specimen from different views are shown in Figure 28.

Figure 27. Pictures of coated tensile test specimens

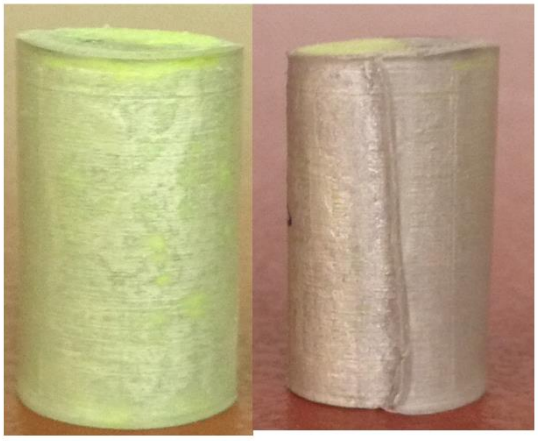

Figure 28. Pictures of coated compression test specimen

After preparing the specimens, the reflective polariscope was placed near the test machine, in order to observe the behavior of the objects under loading. A picture of this experimental setup is shown in Figure 29. Photostress tests were recorded by using a camera. This way stress distribution at every time step could be analysed if necessary. During the test, the change in stress distribution could be observed. In addition to that just before failure, the color of that region showed an abrupt change and failing occurred.

Prior to analysis, calibration of the reflective polariscope was done by following the steps that was indicated by [38]. In order to load the specimens, Zwick/Roell Z020 machine was used and the strain distribution under loading was observed by using photostress method. The moving rate of the upper plate was 3mm/min as before and the experiments were conducted in room temperature, which was approximately 20 °C. During the experiment, in order to observe the load, the screen of the computer was placed right behind the testing specimen. By doing so, it was ensured to note the maximum load under which the specimens fail. This way, the maxiumum load can be compared with the previous tests results.

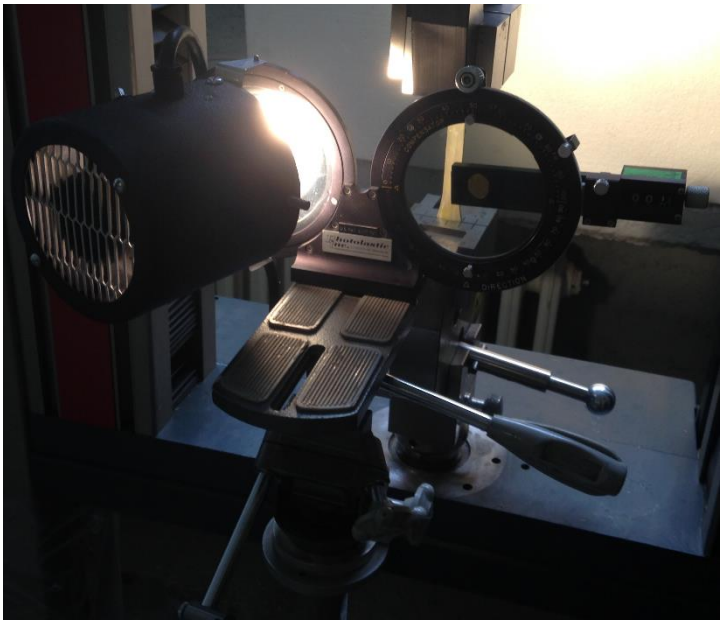

Figure 29. A picture of photostress test setup

2.1.4.2. Photostress Test Results

A qualitative analysis was done by using photostress method. It was observed that the maximum load under which compression specimen failed was increased by 2%. This increase could result from the coating. As explained earlier, in order to conduct the photostress test, the objects should be coated with a birefringent material and this coating layer may have strengthened the compression test specimen. During the compression test, the stress distribution on the object could be observed clearly. After the test, the recording was investigated in detail and the change in color of critical region was observed clearly. The photostress test result for compression specimen is displayed in Section 2.3.4 and the results are compared with the numerical analysis results.

For the tensile test specimen the maximum load at which it ruptures fell within the range of minimum and maximum force values that was observed during the previous tensile tests. Compared to the compression test specimen, the stress distribution on

the tensile test specimen could not be seen very clearly. However, when the test recordings was investigated, similar to compression specimen, the change in color in the failing region was detected.

The photostress test result for tensile test specimen is shown in Figure 30 and from the figure it can be seen that there are some regions with different colors indicating the different strain distributions on these regions. However, the results are not as clear as wanted.

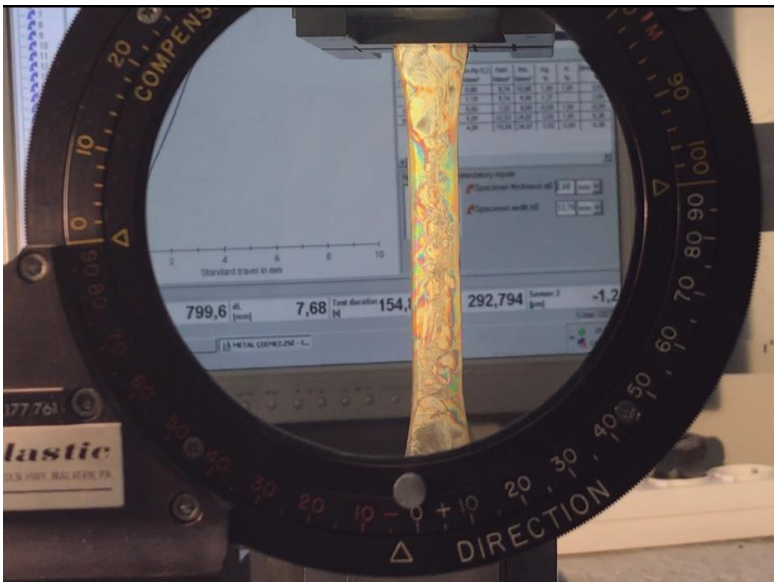

Figure 30. Photostress view of tensile test specimen right before failure

2.2. Numerical Modelling for Compression and Tensile Tests

It is important to verify the experimental results with numerical modelling. The both methods are complementary to each other. In this chapter numerical modelling for compression and tensile tests are done. For numerical analysis, ANSYS Workbench 17 was used and Static Structural module was chosen. The drawings were prepared by using ANSYS Design Modeler.

2.2.1. Numerical Modelling for Compression Test

2.2.1.1. Numerical Modelling Process

The first step of numerical analysis is to draw the part. In the experimental part, compression tests were done by using specimens with two different infill percentages. Therefore, two different parts should have been drawn. Drawing of the fully solid specimen was straight forward. By using the dimensions specified for the compression test specimen, the part was drawn. On the other hand, since the interior section of the other specimen had infill percentage of only 20, the fully solid part should be emptied by 80%. In order to be consistent with the printed part, the parameters from the slicing software, namely Cura, were used. These parameters are given in Table 6. It should be noted that, top/bottom thickness property indicates the thickness of layers which have the infill percentage of 100. In other words, first eight and last eight layers of the specimen are fully solid and the section in between is 80% hollow.

Table 6. Cura infill parameters

Property	**Value**
Infill density	20%
Infill pattern	Grid
Infill line distance (mm)	4
Infill layer thickness (mm)	0.1
Infill line width (mm)	0.4
Top/bottom thickness (mm)	0.8

By using these parameters, the interior side of the fully solid specimen was emptied. The resultant cross-sectional view of the specimen with 20% infill is presented in

Figure 31. Also the cross-sectional view taken from Cura was presented in Figure 32 to show the similarity between the drawn model and the actual geometry.

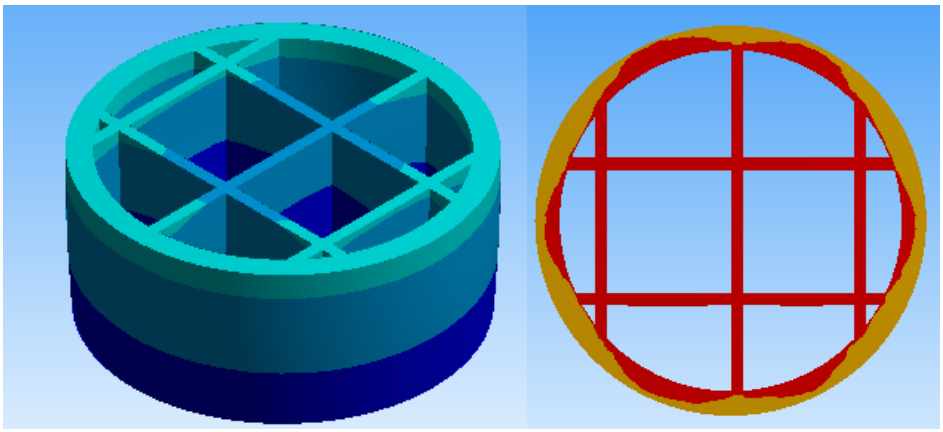

Figure 31. Cross-sectional view of the 20% infill cylinder specimen

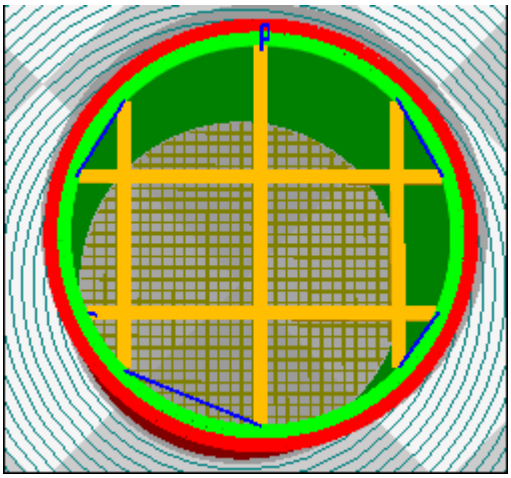

Figure 32. Cross-sectional view of the 20% infill cylinder specimen taken from Cura

After the drawing of the parts were completed, material properties should have been assigned. While printing the specimens, PLA was used; thus, PLA was chosen as the material to be used in the simulations. The experimental results indicated that infill

percentages had a significant effect on the mechanical properties of the material and for different infill percentages, Young's modulus and yield strength values were different. To be consistent with the experiments, for each specimen, the results obtained from the tests were used for these properties. In other words, the results, that were tabulated in Table 3 were used for each specimen. In ANSYS, there are two options to model the behavior beyond yield strength point. One of them is the bilinear isotropic hardening, in which the yield strength and a tangent modulus, which represents the slope of stress-strain in plastic region, are defined. The other method is multilinear isotropic hardening. In this method, one can specify ten strain-stress value, starting from zero as strain and yield strength as stress. By using this method, the material property can be defined more accurately for materials showing non-linear behavior in plastic region. For seven of the specimens, bilinear isotropic hardening method were used. However, for three of the specimens which have 20% infill, the behavior in plastic region observed to be non-linear and therefore the latter method was used. In the experimental part, the strain in transverse direction couldn't be calculated and therefore Poisson's ratio could not be found. Strain gauges were required in order to measure the strain in the transverse direction; however, the specimens were too small to insert strain gauges. As a result, the Poisson's ratio value was taken from the literature [39].

After assigning the proper material properties, the model was meshed. The accuracy and stability of the numerical computation are highly dependent to the mesh quality; therefore, meshing is one of the crucial parts of the numerical analysis. Aspect ratio is one of the parameters that shows quality of the mesh. Lower aspect ratio indicates better mesh quality. The maximum aspect ratio which is recommended by ANSYS is 20. Different meshing properties were obtained for specimens with different infill percentages due to the difference in the interior section of the part. The element size was chosen as 0.45 mm and as a result the number of elements is 195879 for 20% infill specimen and 52864 for 100% infill specimen the number of nodes is 316741 for former and 223763 for the latter. The maximum aspect ratio for 100% infill specimen was 1.54 and for 20% infill specimen it was 9.33. A detailed view of meshed region for 20% infill cylinder specimen is shown in Figure 33.

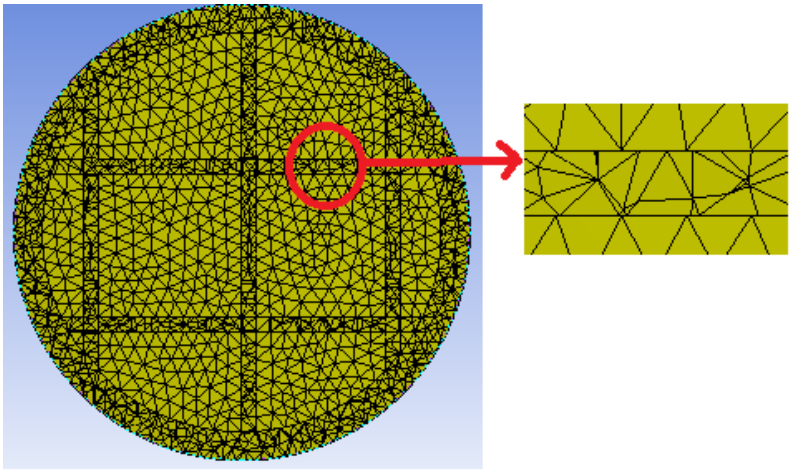

Figure 33. Detailed mesh view of 20% infill cylinder specimen

In the experimental setup, upper plate moved with constant speed, the lower plate was fixed and the specimen was placed in between. To model the movement of the upper plate, constant displacement was defined over a certain time span. In the experiment, the feed rate of the upper plate was set as 3mm/min. During the tests, it was observed that the specimens failed under different displacement values. These values changed in the range of 1.12-1.44 mm for 20% infill specimens; whereas the range was 1.46 to 1.6 mm for 100% infill specimens. Therefore, for each specimen the corresponding failing displacement was applied on the upper surface of the specimens over the corresponding fai1ing time, which was around 30 seconds. Fixed support was defined to the lower surface of the specimen to model the fixed plate under the specimen.

2.2.1.2. Numerical Modelling Results

2.2.1.2.1. Specimen with 20 Percent Infill

During the analysis, the conditions of the compression test were tried to be simulated. The example equivalent stress result for Specimen 1 is shown in Figure 34. In addition, the equivalent stress results from the middle region and the transition region from 100% to 20% infill are presented in Figure 35.

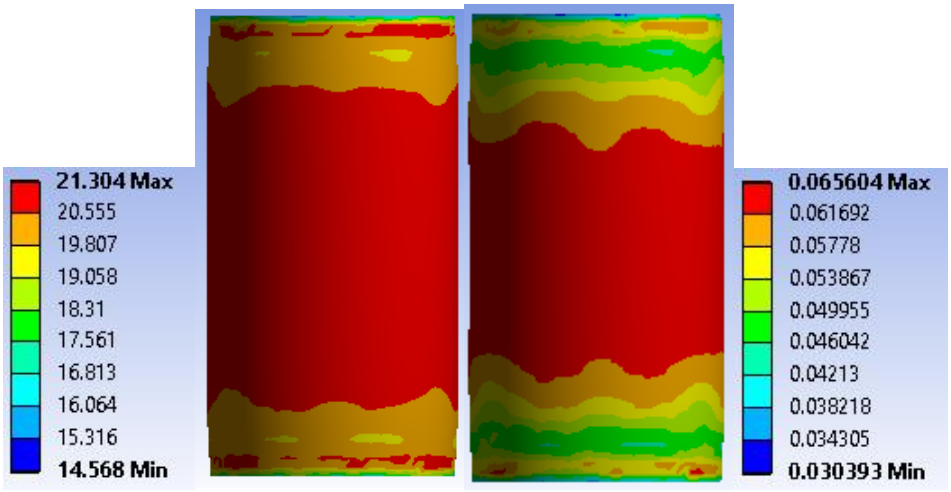

(a) (b)

Figure 34. (a) Equivalent stress (MPa); (b) Total equivalent strain (mm/mm) result for 20% infill cylinder specimen at the end of analysis

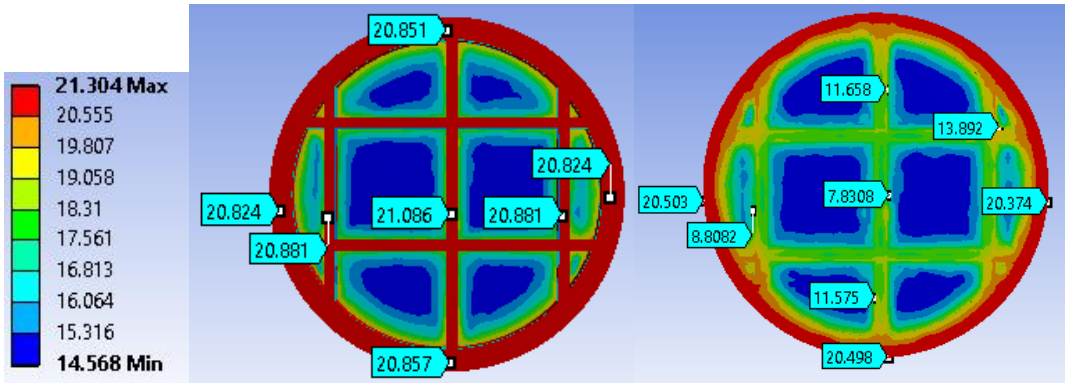

(a) (b)

Figure 35. Equivalent stress results (MPa) for 20% infill cylinder specimen from cross sectional views (a) middle region, (b) the transition region from 100% to 20% infill

It can be observed from Figure 34 that the regions of maximum stress distributions are middle, upper and bottom parts of the specimen. Since the stress is greater than the yield strength, the part fails. From Figure 35, it can be seen that in the middle region all points have similar stress values, yet the center point has the greatest stress value. When the stress distribution on the transition region from 100% to 20% infill

was investigated, it can be concluded that the maximum stress value occurred on the peripheral of the specimen and it decreases towards the center. Moreover, the maximum stress value is very close to the one observed in the middle region. During the compression test, it was observed that out of 5 specimens, 2 of them failed from the bottom and 3 of them failed from the middle. This shows that analysis results show similarity with the tests results and the stress distributions are similar. Failure from different regions may be resulted from the slight differences in the interior section of the specimens. The infill characteristics applied by the slicing program may also show small variations.

To see the effect of loading on the part, the undeformed and deformed models are presented in Figure 36. In fact, the change in shape of the model looks similar to the failed specimen after the compression test.

The analysis was repeated by using the average mechanical properties, which were obtained from the experimental results. The resultant stress-strain graph is presented in Figure 37. The numerical analysis results and experimental results are compared for each specimen and the results are displayed in Section 2.3.1.1.

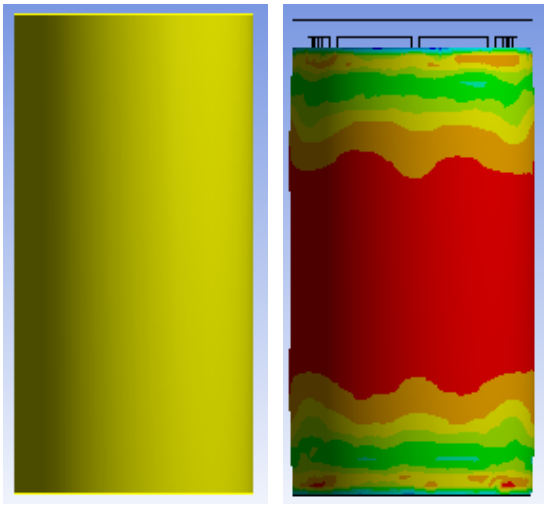

(a) (b)

Figure 36. (a) Undeformed model (b) Deformed model

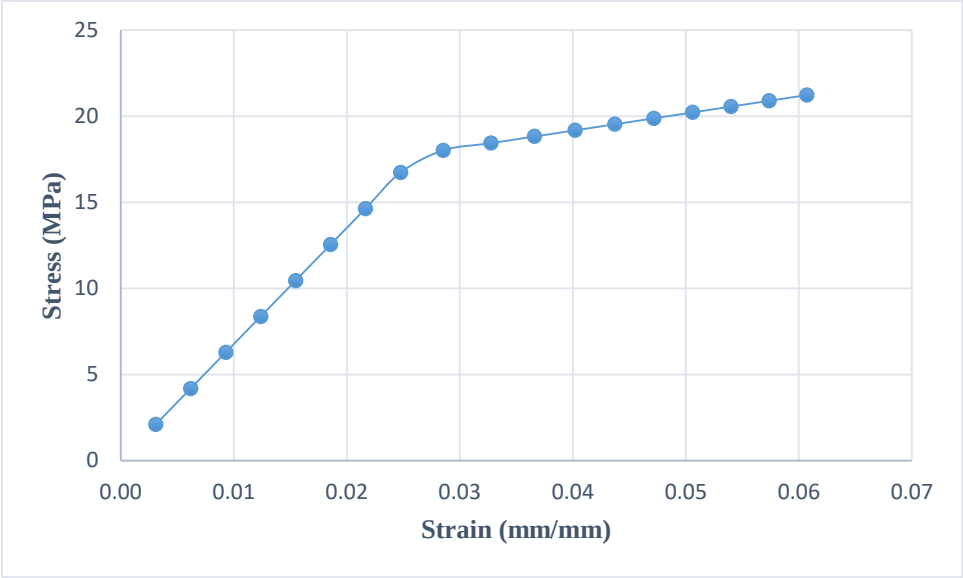

Figure 37. Stress-strain result for average mechanical properties of 20% infill cylinder specimens

2.2.1.2.2. Specimen with 100 Percent Infill

Similar to the previous analysis, the conditions of the compression test were tried to simulated and the equivalent stress result for Specimen 1 is shown in Figure 38.

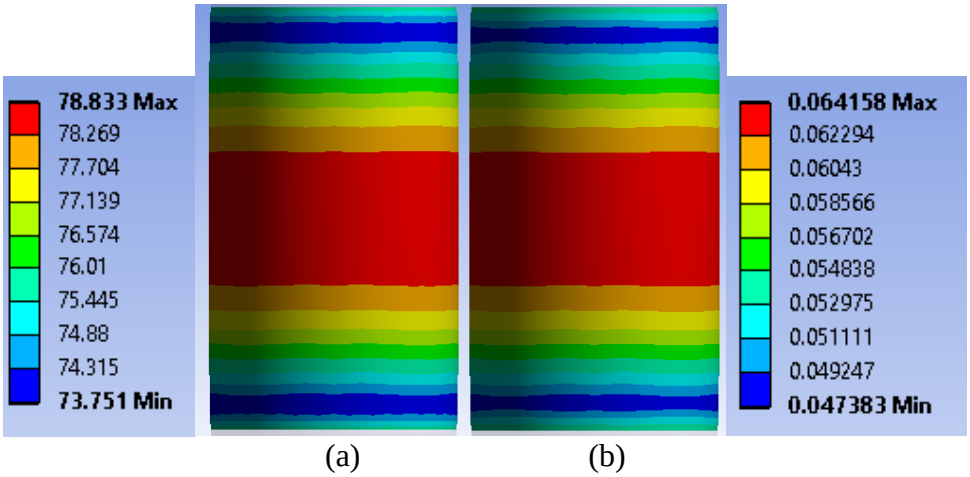

(a) (b)

Figure 38. (a) Equivalent stress (MPa); (b) Total equivalent strain (mm/mm) result for 100% infill specimen at the end of analysis

From Figure 38 it can be seen that the regions of maximum stress distributions are middle, upper and bottom parts of the specimen. The stress accumulation near the upper and bottom part of the specimen can be result from the interactions between the specimen and the upper and lower plate. According to the analysis, small deformations near the upper and lower sections should have been observed; however, there were no indication of that in the tests. During the compression tests, it was observed that all 5 five specimens failed from the middle. Yet, for some of the specimens the failing region was close to upper part, whereas for the others it was close to bottom part. The numerical analysis showed that stress value increased towards the middle and it was greatest in the middle. Therefore, this region should have been the region of failure. The reason of different failing regions can be the slight dimensional and constructional differences between the specimens. Even though all of the specimens were printed at the same time and under the same conditions, they were not completely the same.

After the analyses were done for all of the specimens separately, the analysis was repeated by using the average mechanical properties, which were obtained from the experimental results. The resultant stress-strain graph is presented in Figure 39.The numerical analysis results and experimental results are compared for each specimen and the results are displayed in Section 2.3.1.2.

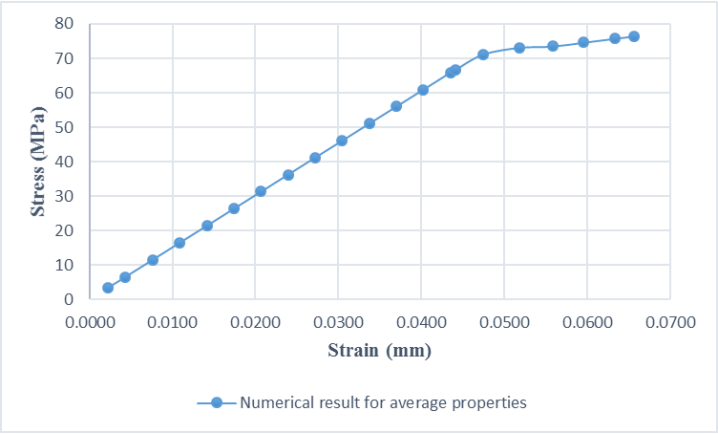

Figure 39. Stress-strain result for average mechanical properties of 100% infill specimens

2.2.2. Numerical Modelling for Tensile Test

2.2.2.1. Numerical Modelling Process

All of the tensile test specimens that were used in the experimental part have 20% infill. Therefore, in order to model the interior part, the parameters from Cura was used. The cross-sectional view for the tensile test specimen is shown in Figure 40. Moreover, the cross sectional view taken from Cura was presented in Figure 41, in order to show the similarity between the drawn model and the actual geometry.

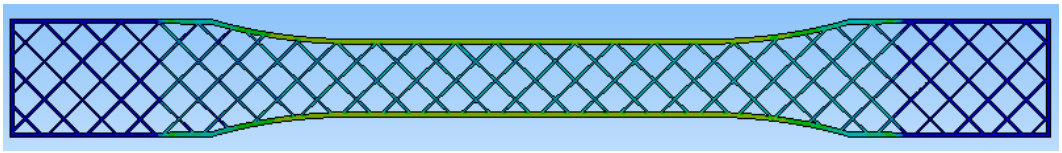

Figure 40. Cross-sectional view of the 20% infill tensile test specimen

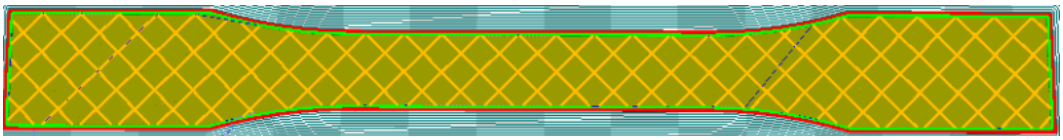

Figure 41. Cross-sectional view of the 20% infill tensile test specimen taken from Cura

After modelling the specimen, material properties of PLA were assigned to the part. The tensile test for each specimen was repeated by using numerical analyses. For each specimen the results which were obtained from the tests and tabulated in Table 4 were used.

Before moving on to the analysis, the meshing was done. For the tensile test specimen, in order to obtain higher mesh quality, virtual topology method was applied. Virtual topology is used to merge small faces together and to simplify small features in the

model. A picture of meshed specimen is presented in Figure 42 and the details of the model mesh are presented in Table 7.

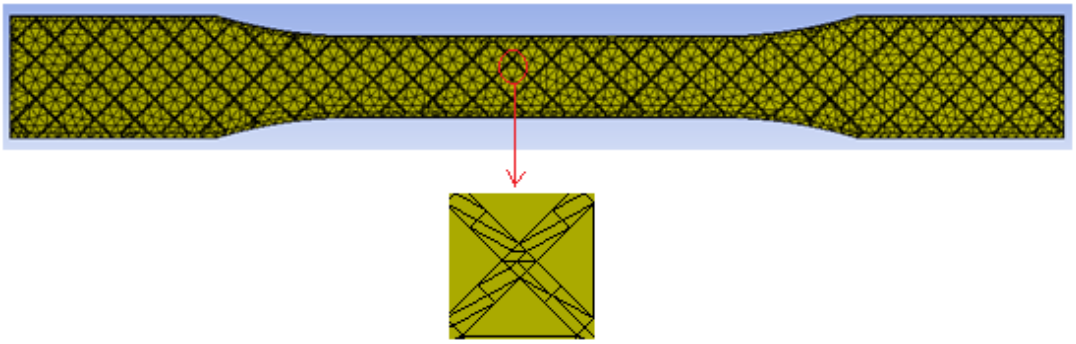

Figure 42. Meshed tensile test specimen and closer view of the meshed wall

Table 7. Details of tensile test model mesh

Property	**Value**
Method	Automatic
Mesh type	Tetrahedron
Body sizing element size (mm)	1.7
Maximum aspect ratio	19.9
Number of nodes	45575
Number of elements	26329

While conducting the tensile test, the specimen was placed between two grippers. To model the effect of grippers on the specimen, faces were created on the upper and lower part of the specimens. The boundaries of the faces were chosen to be 25 mm away from the lower and upper edges. Fixed support was defined on the lower part

and displacement was defined on the upper part. The tensile test specimen model with defined boundary conditions can be seen in Figure 43.

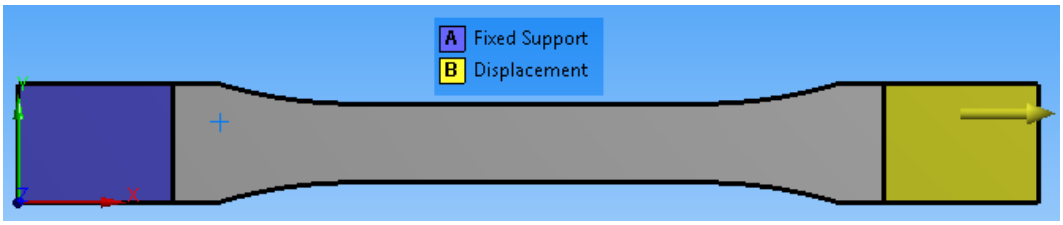

Figure 43. Tensile test specimen model

For the tensile tests, the analyses were conducted by taking the fracture point in the experiments as reference.

After modelling a whole tensile test specimen, an analysis was done for two half specimens which were bonded by using an adhesive. This analysis was done in order to verify the characteristics of the adhesive. First step of modelling was to draw the half specimens. The half specimens were also drawn by using the parameters in Cura. After that, a face was constructed between the parts and 0.1 mm of thickness was defined, which is the adhesive layer thickness. The experimental results for the adhesive was used.

While modelling the adhesive layer between two half specimens, 502CAE was used. 502CAE was decided to be used for the model as a result of the experiments done in the previous chapter. Young's modulus and yield strength of 502CAE were determined by using tensile tests. For the other unknown mechanical properties of this adhesive, its material data sheet was used [40]. The representative figure of two half specimens and the adhesive layer can be seen in Figure 44.

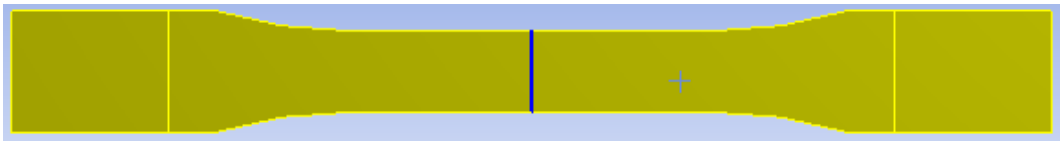

Figure 44. Half specimens and adhesive layer

During the tensile test, it was observed that the failure of the specimen occurred when about 1.5 mm displacement was applied. This condition was defined for the model as well.

2.2.2.2. Tensile Test Modelling Results

By using numerical analysis, the conditions occurred during the tensile test were modelled and. as an example the equivalent stress results for Specimen 1 is shown in Figure 45.

It can be clearly seen from Figure 45 that maximum stress occurred in the middle region. Moreover, it can be interpreted that the stress distribution was symmetric according to the center region and stress value increased towards the center of the specimen by reaching the maximum value in the center. As a result, from this region the specimen should have been failed. However, the test results showed that only one of the specimens failed from the near middle region and the rest failed from different regions. This may be resulted from the small differences between the dimensions of the specimens. In addition to that, interiors of the specimens are slightly different from each other due to the slicing program and this may result in failure from different regions. When the total strain graph in Figure 45 is investigated, such a profile may result from the gaps in the interior part of the specimen. Also, when the dimensions of the specimen were considered, it makes sense that the region with higher stress and strain is the region with smallest dimensions and therefore, it is the weakest region.

To present the deformation of the specimen, the deformed model is shown with undeformed wireframe in Figure 46. It can be seen from Figure 46 that only a small reduction in width of the specimen occurred similar to the result of experimental tests.

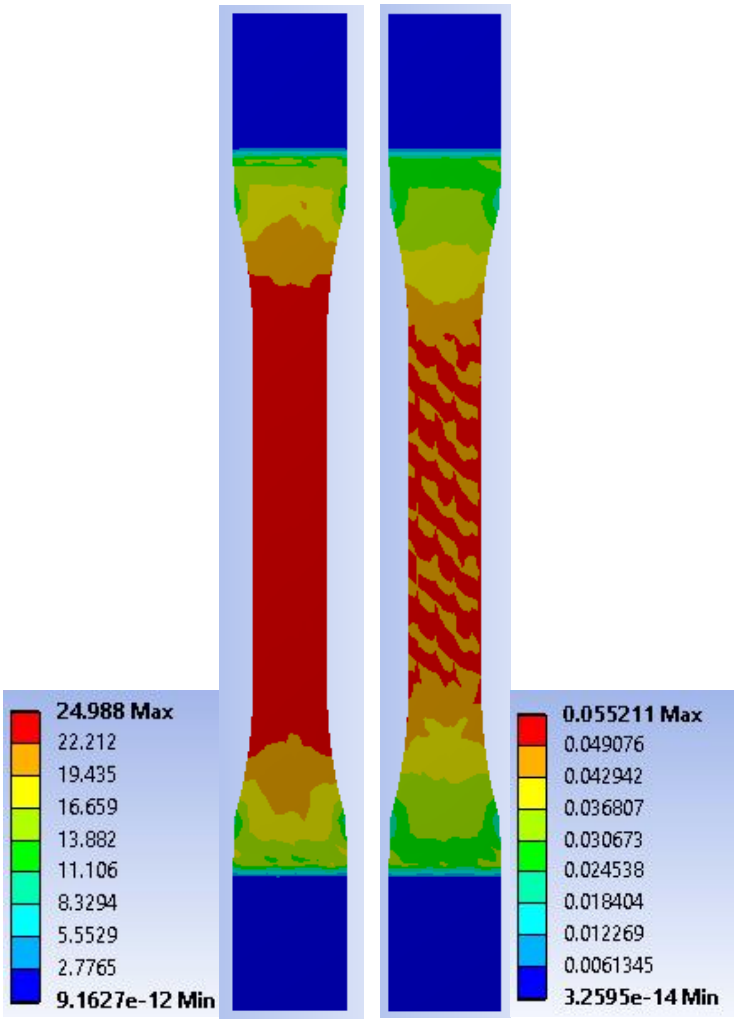

Figure 45. Equivalent stress (MPa) and total equivalent strain (mm/mm) result for tensile test specimen at the end of analysis

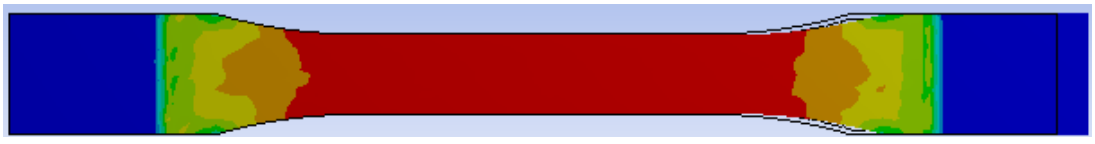

Figure 46. Deformed model with undeformed wireframe

The stress distribution for half specimens bonded by 502CAE and over the adhesive layer cross section are presented in Figure 47. From Figure 47, it can be clearly seen that the maximum stress occurred on the adhesive region. The stress values over the rest of the part were smaller than the yield strength of the PLA and therefore it can be concluded that no failure of the specimens occurred. When the stress distribution over the adhesive cross section was examined, it can be seen that the maximum stress occurred at the corners of the specimen. In other words, the corners were the critical points and the failure of the adhesive layer occurred from these points.

The comparison of the numerical analyses results and experimental results are done in Section 2.3.

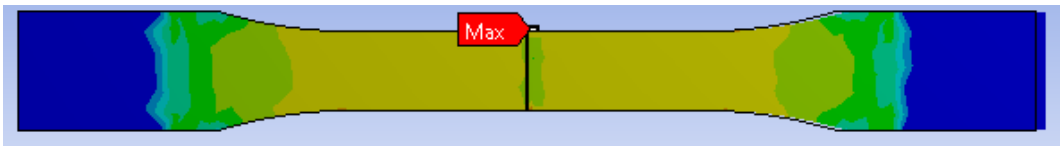

(a)

(b)

Figure 47. (a) Equivalent stress distribution; (b) Stress distribution over adhesive layer cross section

2.2.3. Mesh Independence Study

In numerical analyses, it is very important that results are independent from the mesh size. Mesh independence study was done for three different models; which are 20%

and 100% infill cylindrical compression test specimens and 20% infill tensile test specimen.

While meshing the 20% infill compression test specimen, the element size was chosen as 0.45 mm. The same analysis was repeated for 0.3 mm and 1 mm element sizes. The difference between the stress results of 0.3 mm and 0.45 mm element sizes was found about 7%, when the result for the finer mesh was taken as exact value. When the stress result of 0.45 mm element size was compared with the stress result of 1 mm element size, the difference increases to 18%.

Similar to 20% infill compression test specimens, for 100% infill specimens the element size was chosen as 0.45 mm. Using 0.3mm and 1 mm element sizes the analysis was repeated. When the result for the finer mesh was taken as exact value, the difference between the stress results of 0.3 mm and 0.45 mm element sizes was found about 3%. The difference between the stress results increased to 16% when 1 mm element size was used for meshing.

For the tensile test specimen, the element size for the meshing was chosen as 1.7 mm. As a result of this meshing, the maximum aspect ratio was found as 19.9, which was very close to the maximum limit. The meshing was done by using 0.8 mm element size, which resulted in maximum aspect ratio of 9.83, total node number of 175107 (which was 3.8 times greater than the node number of used element sizing of this study) and element number of 99403. When the stress results of these to different element sizes, the difference was found as only 0.6%.

2.3. Comparison of Experimental and Numerical Analyses Results

2.3.1. Compression Tests

2.3.1.1. Specimen with 20 Percent Infill

The experimental and numerical analyses results for each specimen were plotted on the same graph. For each specimen the corresponding stress-strain results are presented separately in the following figures.

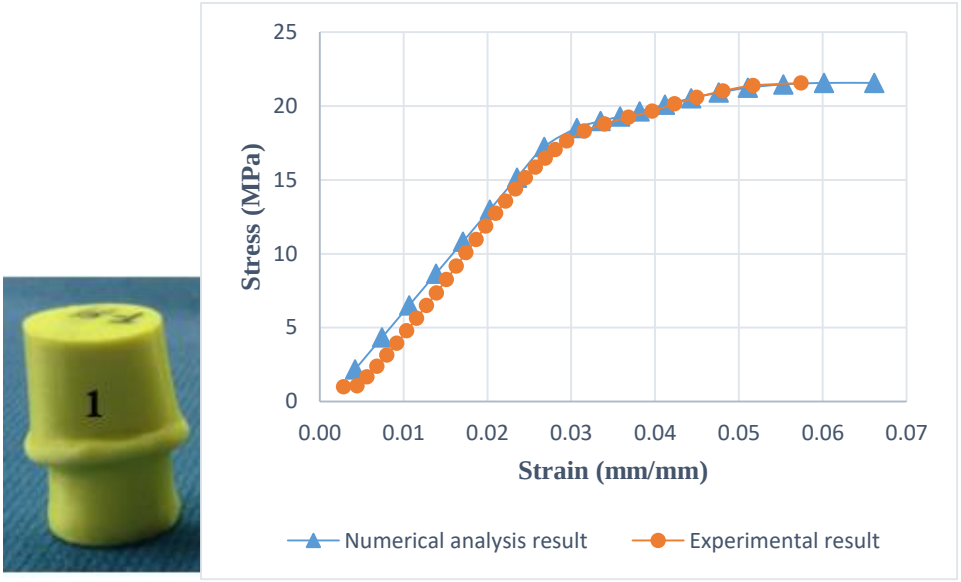

Figure 48. Stress-strain graph showing numerical analysis and experimental results of 20% infill cylindrical compression test Specimen 1

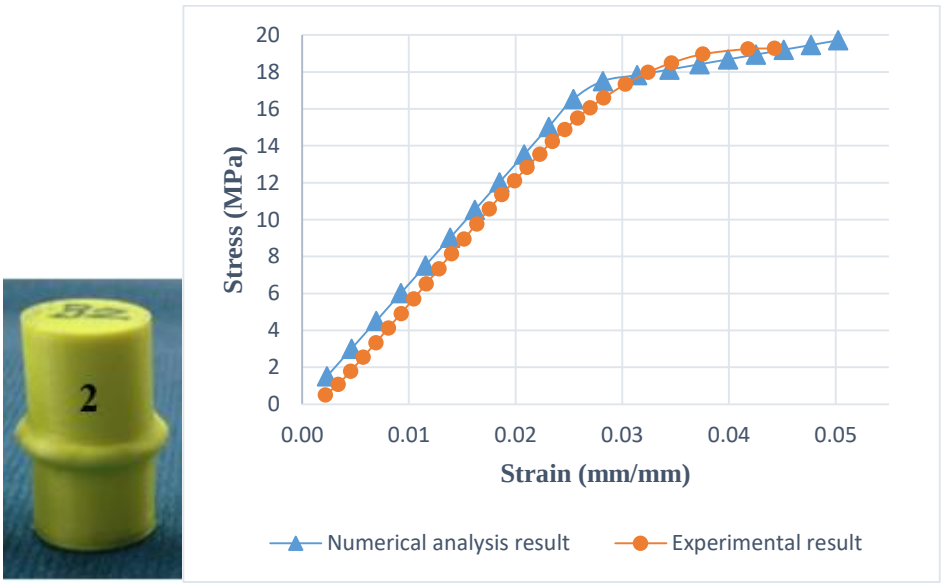

Figure 49. Stress-strain graph showing numerical analysis and experimental results of 20% infill cylindrical compression test Specimen 2

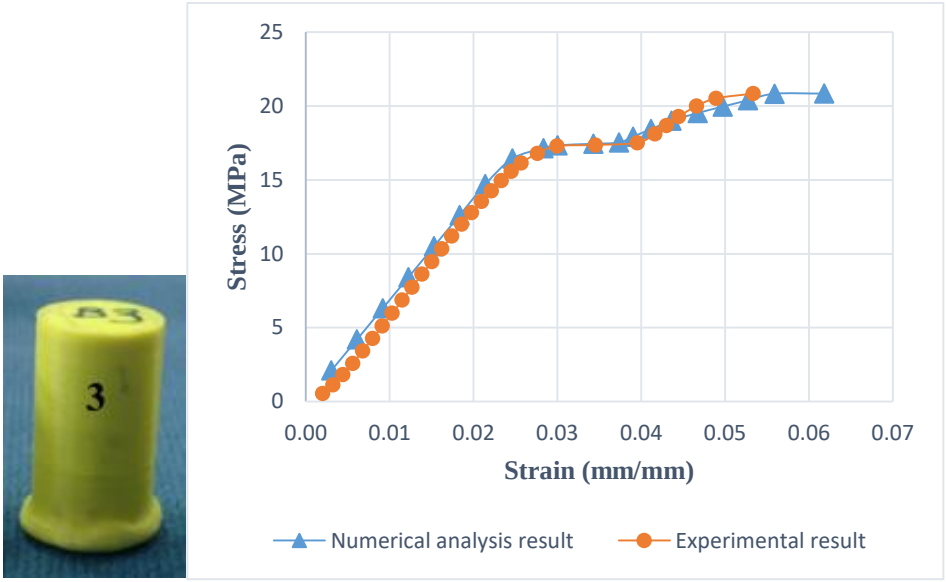

Figure 50. Stress-strain graph showing numerical analysis and experimental results of 20% infill cylindrical compression test Specimen 3

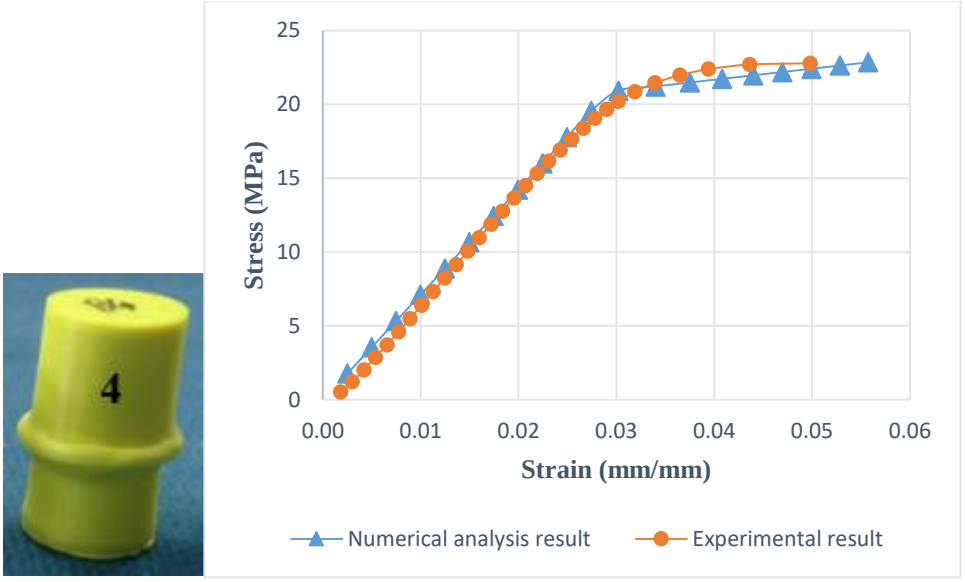

Figure 51. Stress-strain graph showing numerical analysis and experimental results of 20% infill cylindrical compression test Specimen 4

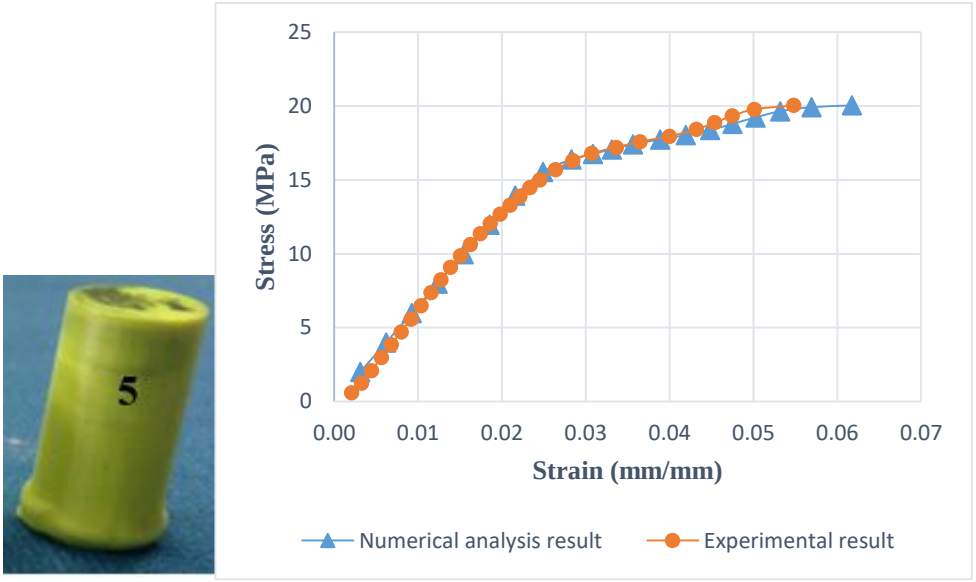

Figure 52. Stress-strain graph showing numerical analysis and experimental results of 20% infill cylindrical compression test Specimen 5

When the figures are examined, it can be seen that the trends of the plots are similar for experimental and numerical analysis results. Yet, one main difference between them can be realized when the figures were closely investigated. From the figures it is very clear that the strain value for the maximum stress is greater for the numerical analyses results by about 10%. This discrepancy may be resulted from the fact that experimental results are calculated by using engineering stress-strain; whereas ANSYS uses true stress-strain values. While calculating the engineering strain, the change in cross sectional dimension is not taken into consideration; whereas in true strain it is. Since the cross sectional area increases under compression loading, the obtained stress value decreases. This situation may cause the difference between the results.

2.3.1.2. Specimen with 100 Percent Infill

The experimental and numerical analyses results for each specimen were plotted on the same graph. For each specimen the corresponding stress-strain results are presented separately in the following figures.

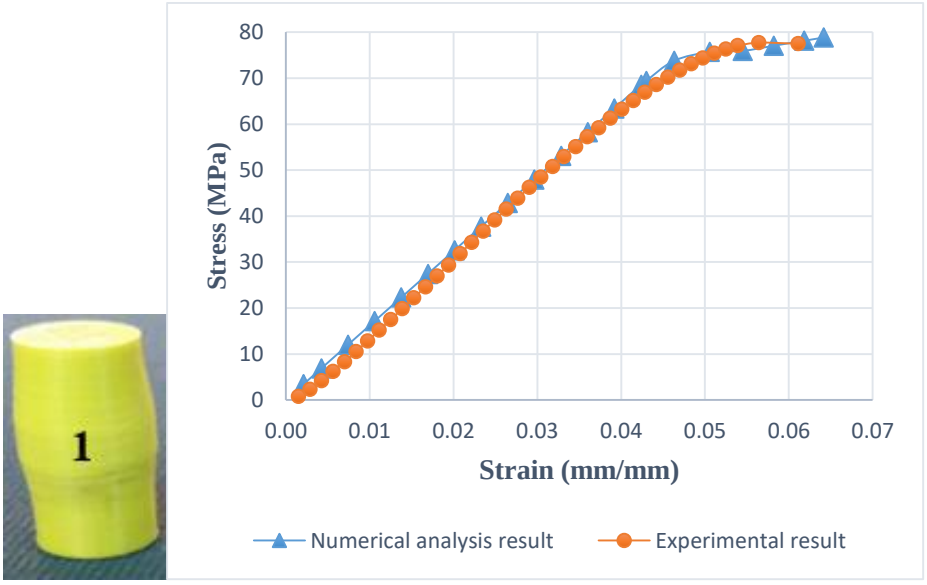

Figure 53. Stress-strain graph showing numerical analysis and experimental results of 100% infill cylindrical compression test Specimen 1

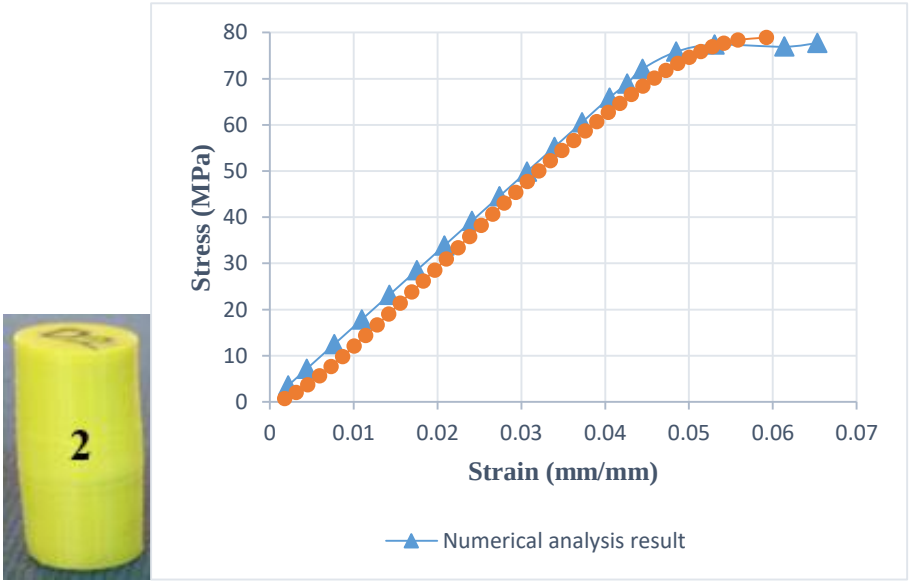

Figure 54. Stress-strain graph showing numerical analysis and experimental results of 100% infill cylindrical compression test Specimen 2

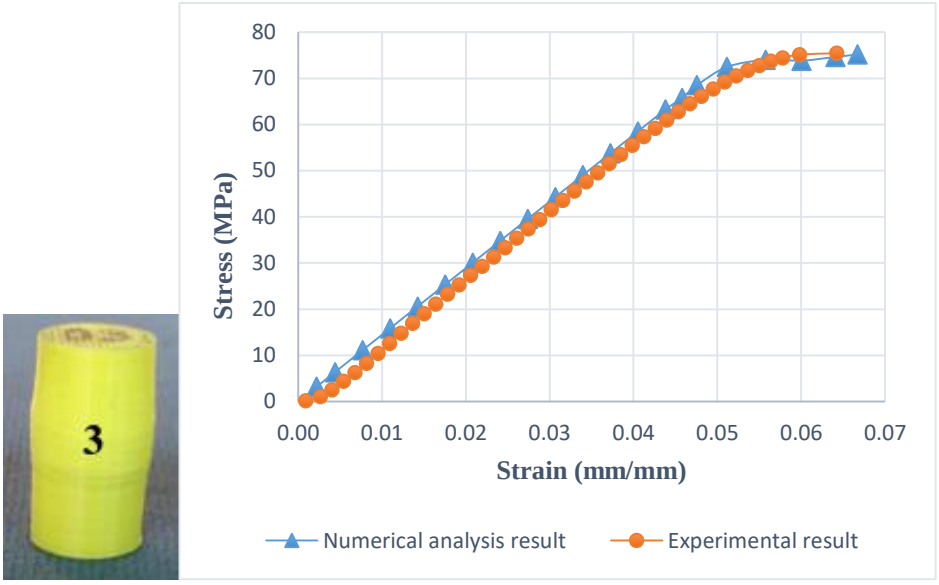

Figure 55. Stress-strain graph showing numerical analysis and experimental results of 100% infill cylindrical compression test Specimen 3

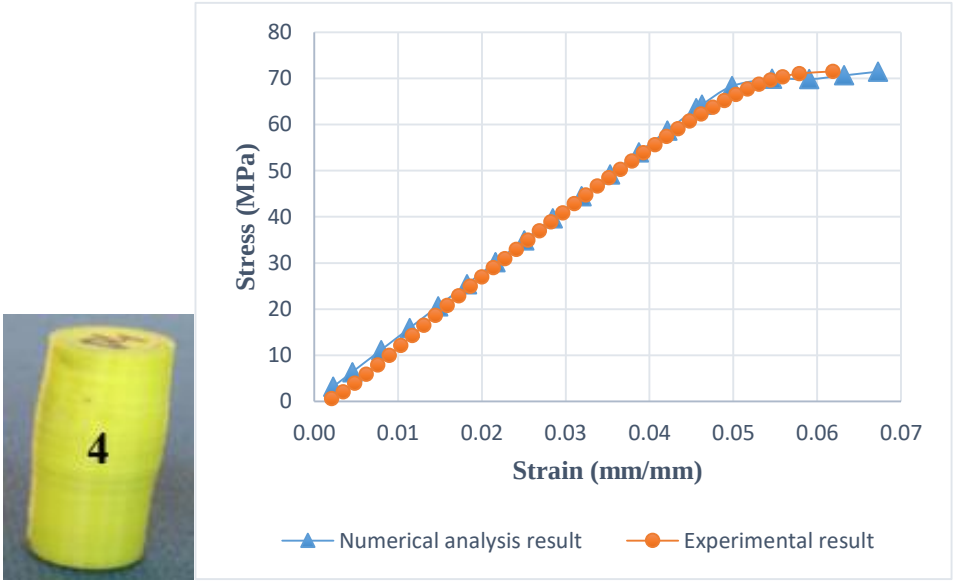

Figure 56. Stress-strain graph showing numerical analysis and experimental results of 100% infill cylindrical compression test Specimen 4

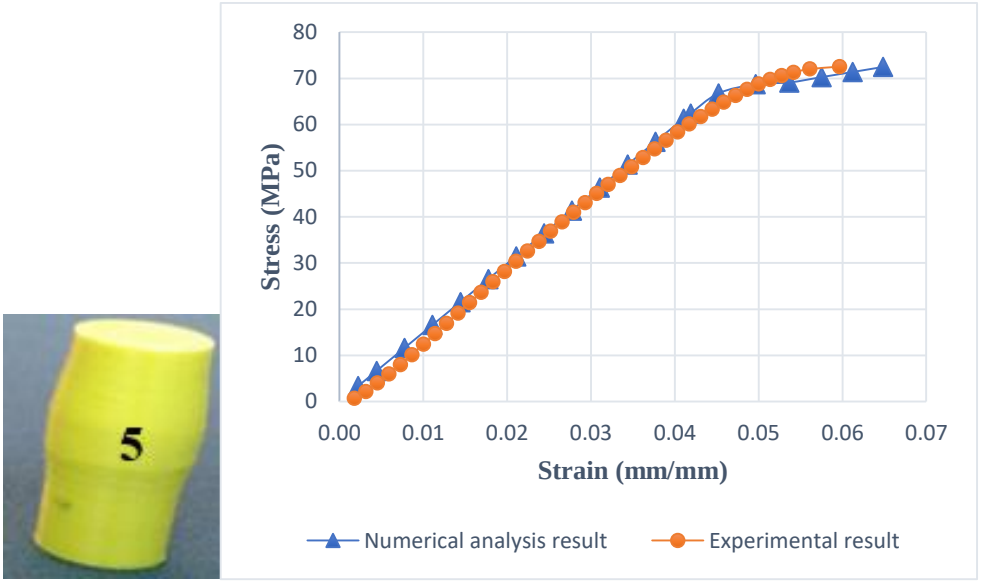

Figure 57. Stress-strain graph showing numerical analysis and experimental results of 100% infill cylindrical compression test Specimen 5

Similar to the 20% infill specimens, the experimental and numerical analyses results for 100% infill specimens match as well. Just as it was observed for 20% infill specimens, the strain value for the maximum stress is greater for the numerical analyses results. This time the deviation between them was about 8%. Moreover, for some of the specimens, this difference was smaller. The reason for this difference was explained earlier. When the deviation percentages were compared with the 20% infill specimens, a decrease can be observed. This decrease can be a result of stiffer characteristics of 100% infill specimens.

2.3.2. Tensile Tests

For the tensile tests, the experimental and numerical analyses results for each specimen were plotted on the same graph. The corresponding stress-strain results for each specimen are presented separately in the following figures.

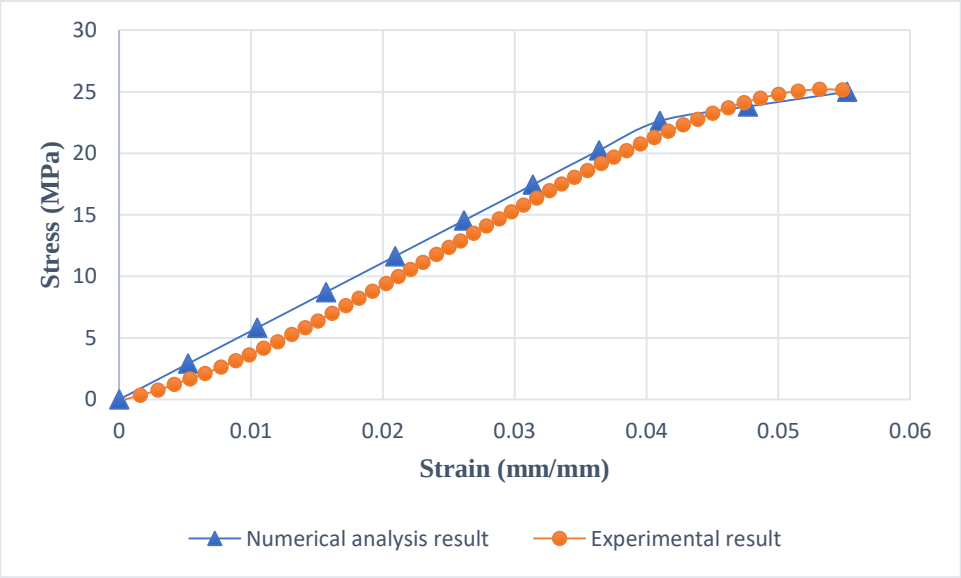

Figure 58. Stress-strain graph showing numerical analysis and experimental results of 20% infill tensile test Specimen 1

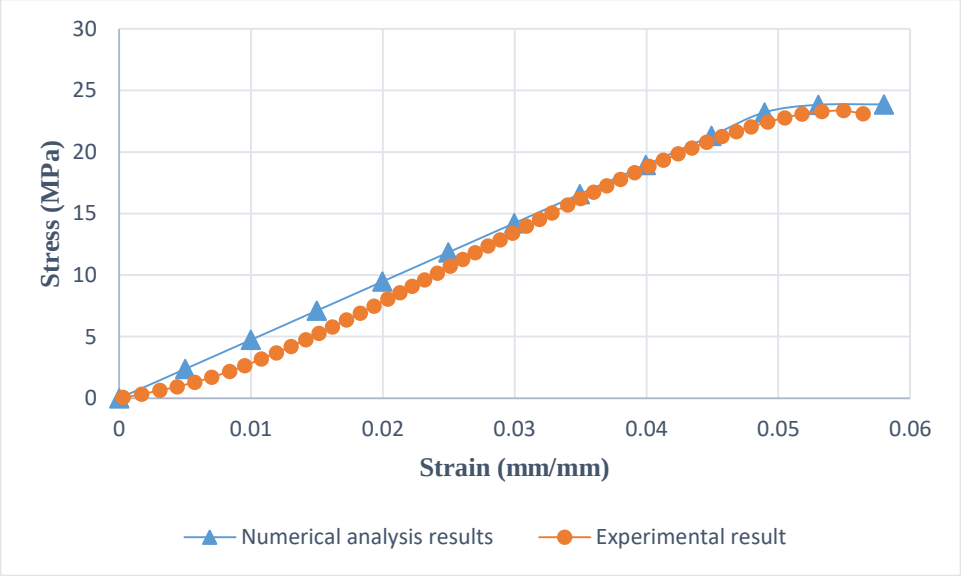

Figure 59. Stress-strain graph showing numerical analysis and experimental results of 20% infill tensile test Specimen 2

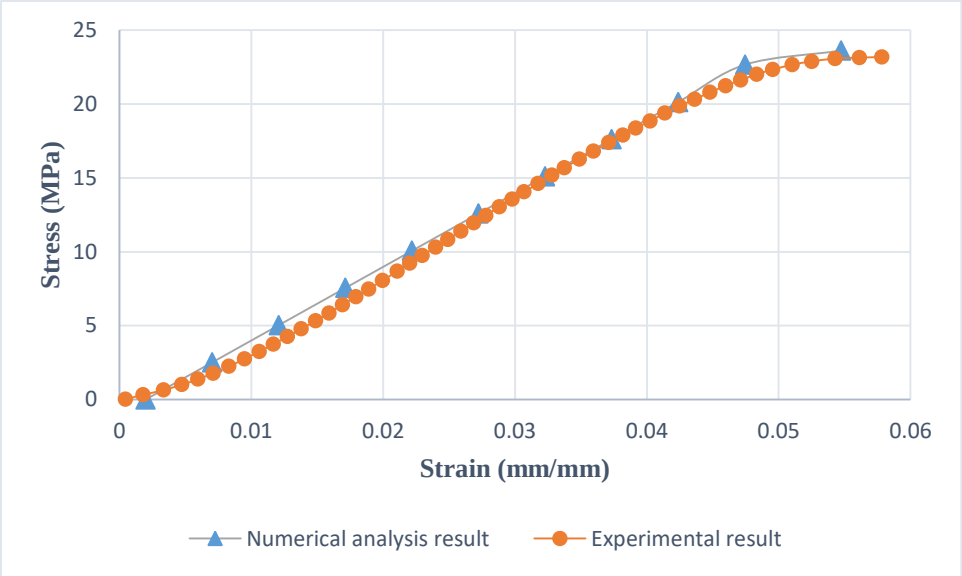

Figure 60. Stress-strain graph showing numerical analysis and experimental results of 20% infill tensile test Specimen 3

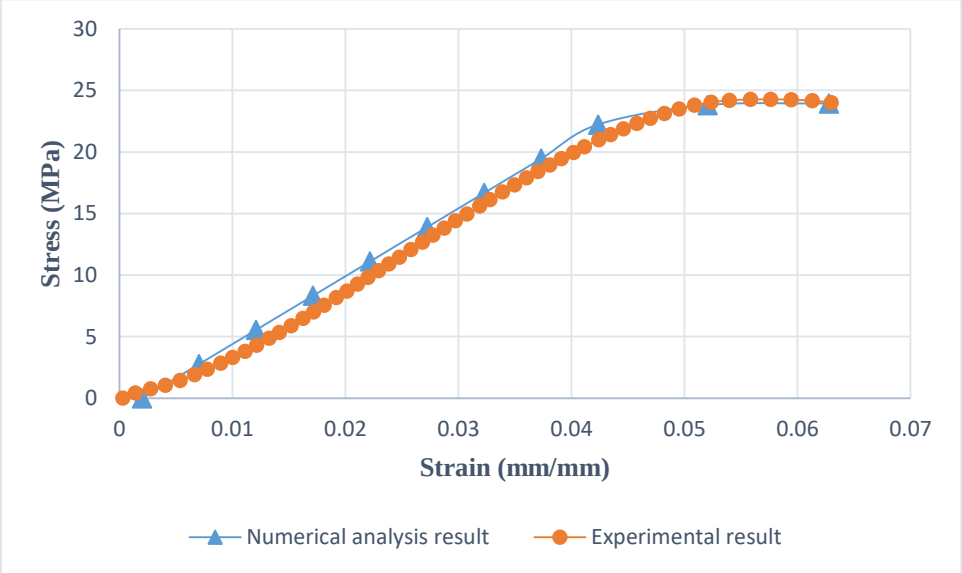

Figure 61. Stress-strain graph showing numerical analysis and experimental results of 20% infill tensile test Specimen 4

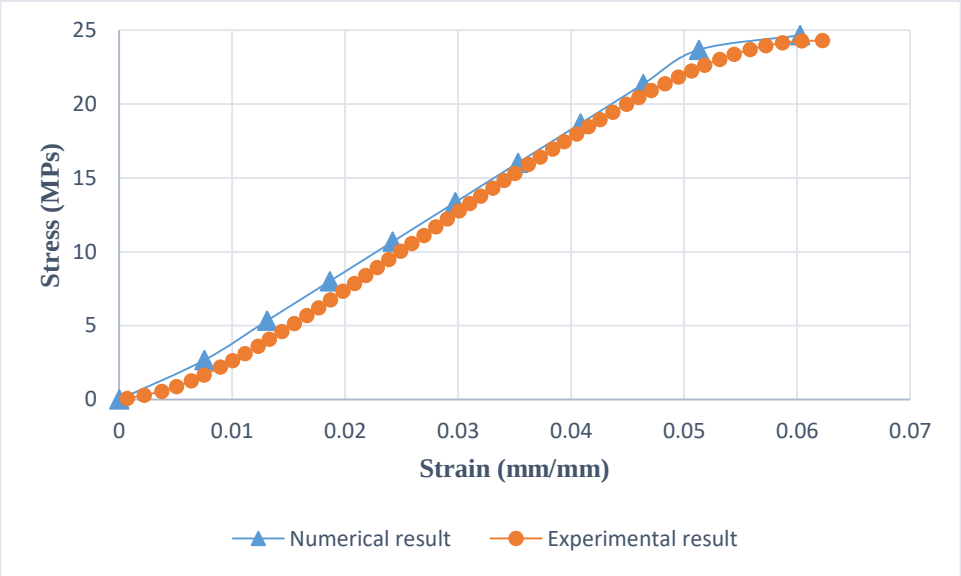

Figure 62. Stress-strain graph showing numerical analysis and experimental results of 20% infill tensile test Specimen 5

It should be noted that the numerical analyses for the tensile tests were done by taking the fracture points of the experiments as reference. In the experiments, the fracture occurred when about 3 mm displacement was applied on the tensile test specimens. However, in numerical analyses, the fracture occurred when about 4 mm displacement was applied. The difference between them is about 25%. This may seem a large value for a discrepancy; however experimental results revealed that even for the specimens printed by using the same filament, at the same time and under the same conditions, the fracture location and maximum stress values change. In addition to that, due to the infill percentage, the sensitivity of the 3D printer effects results significantly. When the filament was deposited layer upon layer, it was assumed that all layers are aligned. However, that may not be the case and for some locations the strength of the object may be reduced owing to imperfectly aligned layers. It is not possible to make a model of this situation and that is estimated as the source of discrepancy.

Similarly, to show the agreement between numerical analyses results and experimental result of the adhesive, they were plotted on the same graph, which is shown in

Figure 63. It can be seen from Figure 58 that for both results, the maximum stress and strain values are nearly the same. Ideally, up to fracture, the stress-strain line should be linear and the slope would give the Young's modulus. However, when the experimental result was examined, it can be observed that the stress-strain line is not linear, rather a curve.

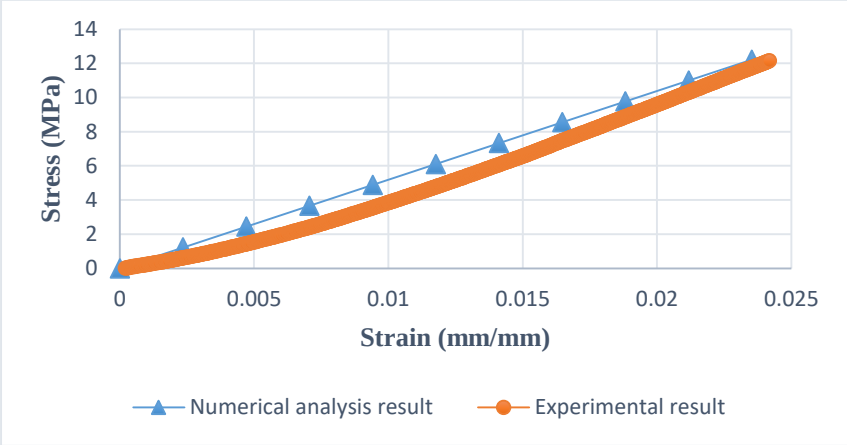

Figure 63. Stress-strain graph showing numerical analysis and experimental results of 502CAE

The similarity between the numerical analyses and experimental results for the adhesive region, indicates that the numerical modelling for the adhesive region gives results which reflects the true behavior of the adhesive. That is a valuable information and can be used for further modelling applications.

2.3.3. Estimation of Mechanical Properties for Different Infill Percentages

In literature, mostly the properties of the bulk material were calculated; however, the properties of objects with different infill percentage were not adequately investigated.

For both compression and tensile test specimen numerical models, it is possible to calculate the Young's modulus of different infill percentages, by using the Young's modulus of the bulk specimens. The infill percentage of the geometry can be adjusted

by defining proper thicknesses to the infill walls. It would be beneficial to estimate the mechanical properties of objects printed with different infill percentage.

Initially, the numerical model was prepared for the compression test. As the first step of the numerical analysis, the mechanical properties of PLA was defined to the geometry. The average Young's modulus of 100% infill compression test specimens, which was 1517.66 MPa, was used for the numerical analyses. After that, the cylindrical compression test specimens were drawn by adjusting the thickness of infill walls, for different infill percentages. To define the displacement boundary condition, the elastic limit of the material was considered; since the Young's modulus can be calculated by using the slope of the stress-strain plot in the elastic region. To make sure to stay in the elastic region, the displacement boundary condition was chosen as 0.6 mm and it was applied over 12 seconds. The displacement value was chosen considering the force displacement diagrams of 20% infill specimens obtained from the experiments, since they have the least strength. To calculate the stress, the force reaction at the fixed support was calculated and divided by the cross sectional area, as it was done in the experiments. To calculate the strain, the displacement was divided by the length of the cylindrical specimen. Then the stress-strain diagram was plotted and the slope of this diagram gave the Young's modulus. This procedure was repeated to determine the Young's modulus of different infill percentages. To determine the yield strength of different infill percentages, linear interpolations between the yield strengths of 20% and 100% infill specimens were done. The average yield strength was found as 17.80 MPa for the 20% infill specimens and 70.71 MPa for the 100% infill specimens. The calculated mechanical properties for different infill percentages are tabulated in Table 8. From Table 8, it can be seen that the estimated Young's Modulus value for 20% infill specimen is 631.33 MPa, which differs from the experimental result by about 7%.

Table 8. Estimated mechanical properties for different infill percentages under compression loading

Infill Percentage	Yield Strength(MPa)	Young's Modulus(MPa)
20%	17.80	631.33
40%	31.03	793.93
60%	44.26	1105.2
80%	57.48	1377.4

Secondly, the numerical analyses were done for different infill percentages of tensile test specimens. The tensile tests were only done by using 20% infill specimens; therefore, the Young's modulus value for the bulk tensile test specimen should be either selected from the literature or should be estimated. As the first option, the Young's modulus from a previous study was used. In a study, which was published on a website about 3D printing, the effect of infill percentage, infill height and infill pattern on the strength of 3D printed objects were investigated [41]. In order to observe the effect of infill percentage on the strength of the object, they produced tensile test specimens with different infill percentages and they found the Young's modulus for the bulk tensile test specimen as 3.1 GPa. This value was selected to be used in the analyses. However, when the Young's Modulus of 20% infill tensile test specimen was calculated, the result was found as 1274.8 MPa, which was about 2.4 times greater than the experimentally found value. There are many parameters that affect the strength of the 3D printed object. The raster orientation, raster angle, deposition directions and layer thickness are some of them. Even the PLA properties may differ from filament to filament. Therefore, it was decided that using a Young's modulus value from the literature may not be appropriate. As a result, a Young's modulus value for the bulk tensile test specimen was estimated. The value was chosen to be 1200 MPa, because when the numerical analysis for the 20% infill tensile test specimen was done by using

this value, the calculated Young's modulus was found to be close to the experimental results. Similar to the compression test numerical modelling, the infill percentages were adjusted by assigning the proper infill wall thicknesses. Also, the stress was calculated by diving the force reaction occurred on the fixed side into smallest cross sectional area and the strain was calculated by dividing the displacement into the length of the test section. The displacement value was chosen to be 2 mm and it was applied over 30 seconds to stay in the elastic region. The calculated stress-strain results were plotted and the slope was used to determine the Young's modulus for different infill percentages. For the yield strength calculations, linear interpolation between the yield strength values for 20% infill and bulk tensile test specimens. For the yield strength value of 20% infill specimens, the average value calculated in the experimental results was used, which was 23 MPa. For the bulk specimen, yield strength value from a previous study done by Song et al. [14] was used. As previously mentioned in Chapter 2, they found the yield strength of the bulk tensile test specimen as 95 MPa. This was a reasonable value when it was compared with the yield strength of the 20% infill specimens found in this study. The calculated mechanical properties for different infill percentages are tabulated in Table 9.

Table 9. Estimated mechanical properties for different infill percentages under tensile loading

Infill Percentage	**Yield Strength(MPa)**	**Young's Modulus(MPa)**
20%	23	493.46
40%	41	660.27
60%	59	801.92
80%	77	1050.1
100%	95	1200

In the previously mentioned study, which was published on a website [41], they investigated the effect of infill percentage on the strength of the 3D printed object. In order to do that, they produced tensile test specimens with different infill percentages. The infill pattern they chose was linear, whereas in this study grid infill pattern was used. Also, for the layer thickness, they used 0.2 mm; on the other hand, it was chosen as 0.1 mm in this study. They used 5 different infill percentages, which are 10, 30, 50, 70, 90 and 100. The Young's modulus values they found were 600, 1000, 1500, 2100, 2900 and 3100 MPa respectively. When the results in Table 9 were investigated, the difference between the results can be seen. As mentioned previously, the difference may be result from the different filament properties, different layer thickness and different infill pattern.

2.3.4. Photostress Test

A qualitative analysis was done by using the photostress method. Strain distribution on the specimen was observed with this method. Different strain values resulted in different colors and the critical regions were determined by using the indicated information of the colors. The photostress test result of the compression specimen under loading, just before the failure is presented in Figure 64 in which the different colored region in accordance with the different strain distributions can be seen clearly.

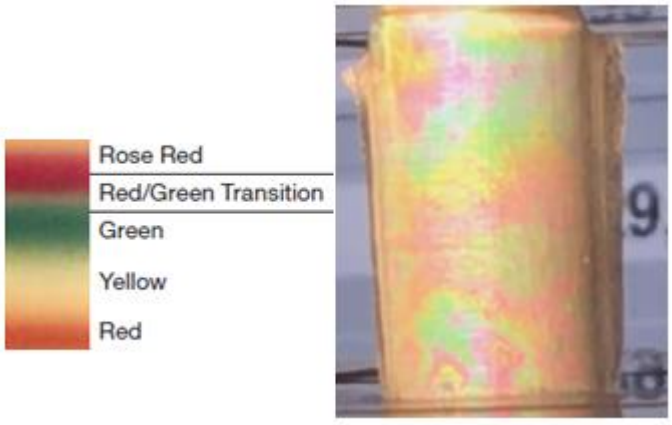

Figure 64. Photostress test result of compression test specimen just before failure

Numerical analysis for the compression test specimen was also done by following the previously mentioned steps of modelling and analysis. After the analysis, the color legend of the total strain result just before failure was adjusted by considering the color schematic in Figure 26.

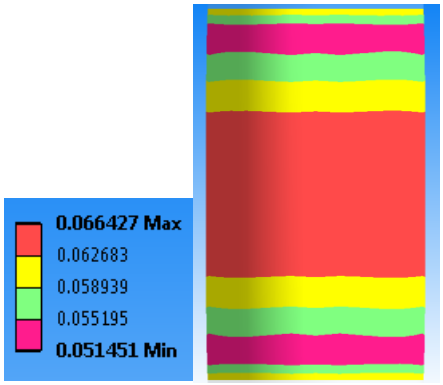

Figure 65. Equivalent total strain result (mm/mm) of compression test specimen just before failure

When Figure 64 and Figure 65 are compared, it can be seen that they are similar to each other. For sure there are some regions in the photostress test result that do not completely look like the numerical analyses result. The difference may result from the coating on the specimen. Even though a uniform reflective paint layer and epoxy coating were tried to be applied, they may not have exactly the same thickness at every point of the specimen. This may cause some error while observing the photostress test result. In addition, since the specimen used for this test has a fully solid interior region, the specimen was assumed to be filled uniformly. Yet, there may be small non-uniformities occurred within the specimen, during the 3D printing process.

CHAPTER 3

CASE STUDY

In Section 3.1 the determination process of the object for the case study is explained. In Section 3.2, the steps for the numerical modelling of the helmet are described and the assumptions are stated clearly. Section 3.3 is dedicated to different numerical analyses done by using helmet and corresponding results are presented.

3.1. Object to be Modelled

One of the aims of this study is to observe the effect of partitioning on the strength of the object by using numerical modelling. In order to do that first the object to be used should be determined. This object should be something useful and something personal. In this thesis, a custom fit motorcycle helmet was decided to be used as a case study. There are two reasons behind choosing the helmet as an example object. Firstly, since everybody has different head sizes, it would be advantageous to print helmets that can fit each individuals head perfectly. However, a helmet is not small enough to fit into the printing volume of a home-use 3D printer and it can only be printed after obtaining smaller sub-parts by partitioning it. Secondly, motorcycle helmet is a very useful object and frequently used in daily life. Actually, motorcycle helmets are very crucial since the majority of the fatal injuries occur in the head during motorcycle accidents [42].

Generally, motorcycle helmets consist of five basic components. These are; a very thin and hard outer shell, a soft and thick inner liner which absorbs the impact, a comfort padding, a visor and a retention system. The parts of the helmet are illustrated in Figure 66.

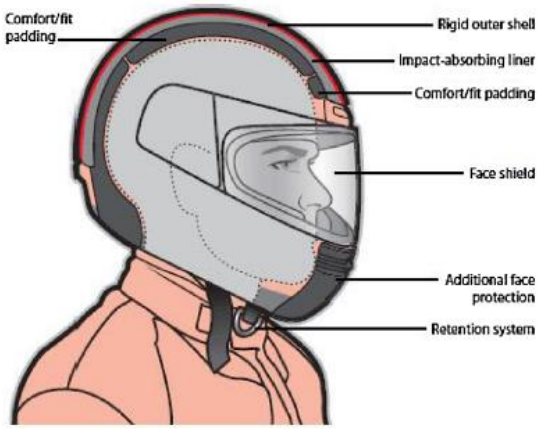

Figure 66. Basic helmet components [42]

Mostly thermoplastic materials like polycarbonate (PC) or ABS are used as the material of the outer shell [42]. Inner liner foam is used in order to absorb the impact force and decrease its effect on the head. Although some of the energy is absorbed by the outer shell, a considerable amount of it is absorbed by the inner liner foam. Most widely used material for the protective helmets is expanded polystyrene (EPS) foam. EPS is a synthetic cellular material and it has great shock absorbing properties with a proper cost to benefit ratio [43].

In order to simulate a motorcycle accident, the direction, the location and the magnitude of the impact should be known. Otte et al. [44] made an extensive research about motorcycle accidents. They collected data from July 1995 to June 1998 in Finland, Germany and United Kingdom by visiting the hospitals, interviewing with the patients and hospital personnel. As a result, they prepared a very detailed report. This report

contained information about the motorcycle accidents, such as the percentage of fatality & injury, type of injuries, type of accidents, type of damages on the helmets, etc. As one of the results of this study, they divided the helmet into seventeen zones and presented a diagram which shows the impact probabilities to each zone. This diagram is presented in Figure 67. From Figure 67 it can be seen that, the right and left chins have the greatest impact probabilities. In fact, the right chin has the greatest probability.

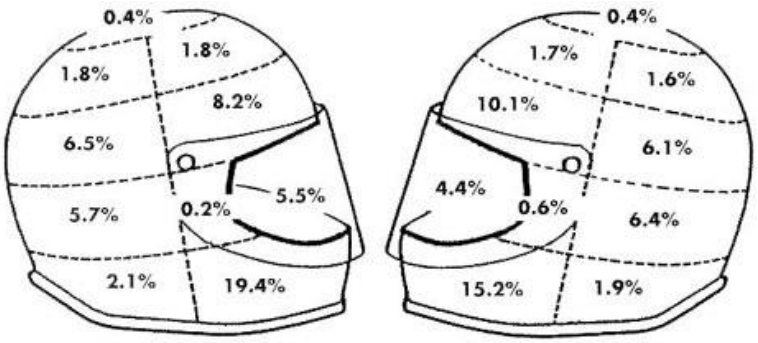

Figure 67. Otte's diagram for impact probability based on post-accident analyses of relatively large data [45]

In addition to the probability results, they also provided information about the most probable direction of impact. According to their report, the most probable direction of impact was the perpendicular direction with a 28.7% probability [44]. Furthermore, they pointed out that the impact, which comes from the perpendicular direction caused the greatest damage on the helmet.

3.2. Numerical Modelling of the Helmet

After 3D printers started to gain popularity among the hobbyists and the number of people who have 3D printers in their homes increase, online sharing of experience and models for 3D printed objects also increased. One of the popular sharing platforms for 3D printing models is Grabcad. In this study, a helmet model which was taken from Grabcad, was used [46]. While numerically modelling the helmet, the regions in

Figure 67 were taken as the basis for partitioning the helmet. Otte's regions were chosen for partitioning sections while, small enough sub-parts that can fit into the printing volume could be obtained as a result of partitioning. The largest parts were right and left chin parts and yet they could fit in the building volume of a home-use 3D printer.

It is not possible to create a computational model which simulates all the complexity in real life. It is essential to make some assumptions during the modelling. In this study the following assumptions were made to simulate the damage on a motorcycle helmet case:

a) In 3D printing the infill percentage is a controllable parameter. For the helmet the infill percentage was chosen as 100% in order to obtain the maximum strength. This was one of the conclusions made in Section 2.1.2.2.
b) The analyses were done by considering the percentages in Otte's diagram and the regions in the diagram were replicated. Since the region areas were not equal, a small common impact area was defined on the centroid of each surface in order to equalize the magnitude of the impact. This rectangular region has a length of 45.15 mm and width of 24.57 mm. A picture of the partitioned helmet model with the defined rectangular regions is shown in Figure 68.

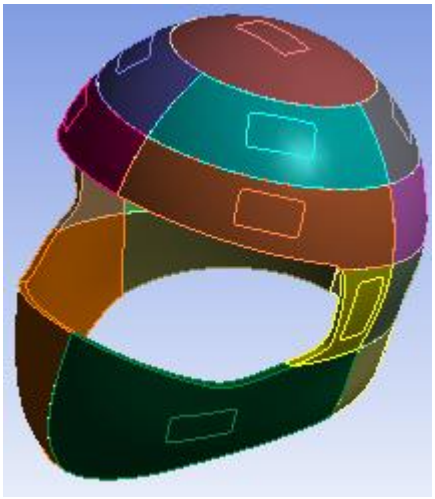

Figure 68. A picture of partitioned helmet model with defined rectangular regions

c) Meshing of the helmet was done by using an element size of 4 mm. This method resulted in an aspect ratio of 15, which was below the advised limit. The number of nodes was 197628 and number of elements was 115317. The detail mesh image on the helmet can be seen in Figure 69. When Figure 69 is examined, it can be seen that near the corner of the rectangular regions, there exist higher mesh density.

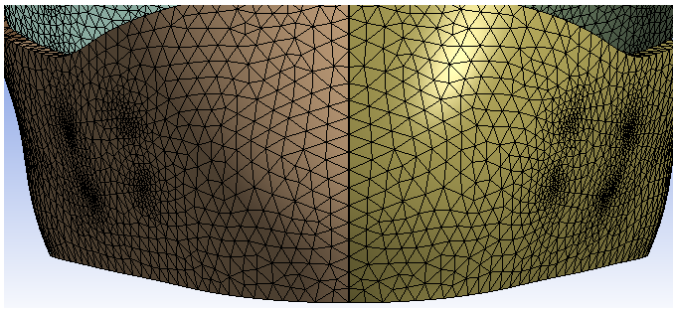

Figure 69. The detail mesh image on the helmet

d) The impulse should be replaced with force distribution, in order to make a steady state analysis. To mimic the impact, pressure on the predefined common rectangular region was defined as a function. This function was defined such that Gaussian distribution is obtained on the rectangular region. Due to Gaussian distribution, the effect of the pressure is greater in the center and becomes smaller with increasing radius. The function is defined as in Equation (1).

$$f(z) = \frac{1}{\sqrt{2\sigma^2\pi}} e^{-\frac{(z-\mu)^2}{2\sigma^2}} \quad (1)$$

In this equation σ is standard deviation, μ is mean and z is the direction. For this application μ is taken as zero and σ is taken as one to obtain the standard normal distribution. Therefore, the Gaussian distribution function simplifies to Equation (2).

$$f(z) = \frac{1}{\sqrt{2\pi}} e^{-\frac{(z)^2}{2}} \tag{2}$$

e) In order to obtain the magnitude of applied pressure value, Equation (2) is multiplied by the impact force and divided by the area of the predefined rectangular region. The impact force value was chosen as 14715 N, since it is the value that Snell Memorial Foundation uses while testing the motorcycle helmets for certification [47]. By using this function, the required pressure distribution was obtained. The pressure distribution is shown in Figure 70.

f) The direction of the impact was chosen to be always perpendicular to the helmet's surface. This assumption was actually based on the fact that the possibility of the helmet to hit by an impact direction of 90-degree angle is the greatest and causes the maximum damage as noted before. The latter will be verified by using numerical analysis in the following section.

g) During an accident, there are many parameters that should be considered. In terms of numerical analyses, it is not possible to realistically model the accident and its effects on the driver. Therefore, this study focuses only on the damage on the helmet. Hence, below the helmet the head or the human body was not modelled. As a result, fixed support was defined to the bottom face of the helmet.

h) To define the adhesive layer, faces were created between the parts to be glued. A thickness of 0.1 mm is then defined to these surfaces, which represents the thickness of the adhesive. The adhesive that was proved to show the greatest performance in Chapter 2, which was namely 502CAE, was used for the adhesive layer modelling. The contact type for the contact regions were chosen as bonded, which was the most suitable type for the adhesive surface modelling.

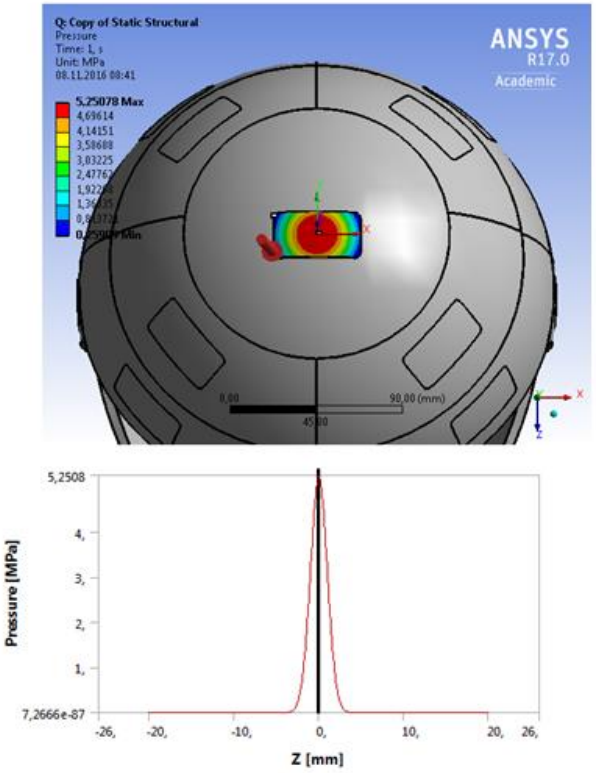

Figure 70. Pressure distribution in impact region

i) Although a helmet consists of many layers, in this study for simplicity only two of them were modelled; which are outer shell and inner liner. To model the inner liner foam, elastic support was defined to the inner face of the helmet. To define the elastic support, Elastic Foundation Stiffness (EFS) should be defined. From the definition, EFS is calculated by using Equation (3).

$$EFS = \frac{F}{x_{efs} \cdot A} \tag{3}$$

In this equation F is force, x_{efs} is the deflection under that force and A is the area on which the force is applied. In this study, the impact force is nearly 15kN and under this force EPS foam with a density of 68 kg/m^3 will deflect 20 mm [48]. Therefore, these values are used to calculate the EFS.

3.3.Analyses and Results

3.3.1. Analyses of Most Critical Impact Direction

According to Otte's report, the most probable regions of impact are the chins. Moreover, he suggested that the direction of impact would be most likely normal to the surface and the impact that occur from this direction cause more harm on the helmet. Therefore, in this study while modelling the impacts on the helmet, all of the directions were chosen as normals to the surfaces.

To illustrate the difference between the effects of shear force and normal force on the helmet, analyses were conducted by using shear forces and normal forces. This analysis was done by assuming the impact occurred on the right chin part. The direction of force, the region on which the force was applied and the corresponding coordinate system was shown in Figure 71.

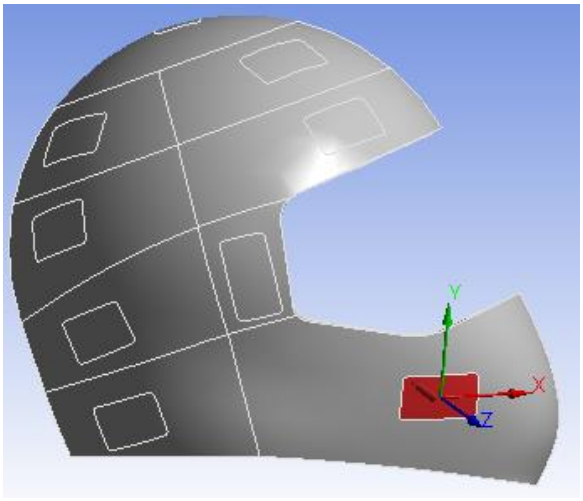

Figure 71. Coordinate system definition

For the analyses the impact region and the magnitude of the forces were chosen to be identical; only the directions of the forces were changed. At first the force was applied from perpendicular direction, which was -z direction according to the local coordinate system. After that, forces were applied from in plane directions which were x and y directions, respectively. The corresponding stress distribution results are illustrated in Figure 72.

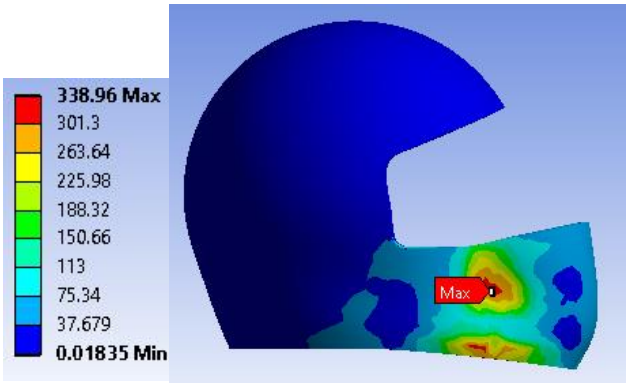

(a) Force applied in -z direction (normal)

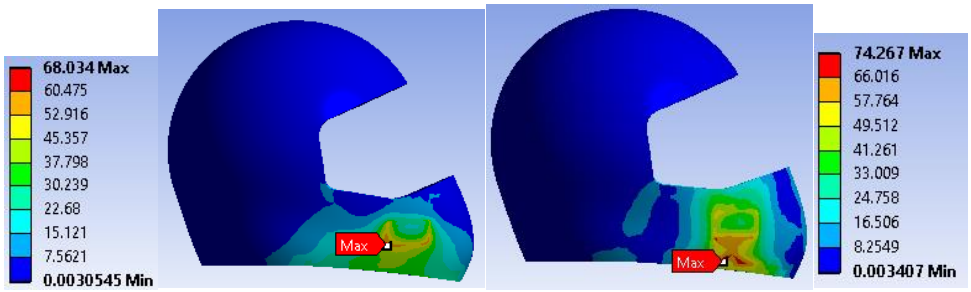

In plane force applied (b) in x direction (c) in y-direction

Figure 72. Equivalent stress results (MPa) for different force directions

As it can be seen from Figure 72, the force applied from perpendicular direction caused the maximum stress on the helmet with 338.96 MPa. This value was almost 5 times greater than the maximum stress value occurred when a force was applied in x direction and 4.6 times greater than the the maximum stress value occurred when a force was applied in y direction.

3.3.2. Analysis of Adhesive Layer

In order to demonstrate that the adhesive shows similar behavior when it was applied on the tensile test specimen, simple numerical analysis was conducted by using the helmet. The top part of the helmet was partitioned, and it was glued to the bottom part by using 502CAE. On the upper surface a boundary condition was defined. such that the same force over area ratio with the tensile test analysis was obtained. The resultant stress distribution over the helmet and the adhesive layer can be seen in Figure 73.

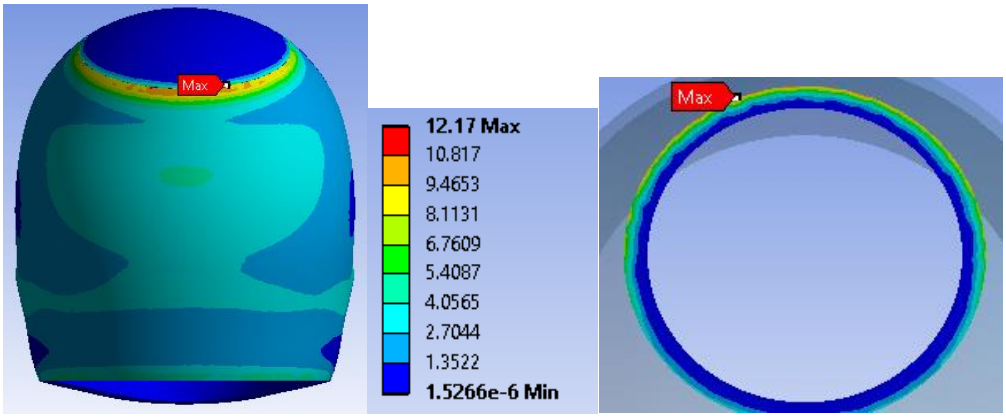

(a) (b)

Figure 73. Stress distributions (MPa) (a) on helmet from back view; (b) adhesive layer from top view

By examining Figure 73, it can be seen that the maximum stress occurred on the adhesive layer with 12.17 MPa. This value which was greater than the yield strength of the adhesive and indicates the failure of the adhesive region. When the stress distribution over the helmet was examined, it can be clearly seen that the maximum stress value was much smaller than the yield strength of the PLA material. Therefore, it can be concluded that when the top part of the helmet was partitioned and glued, the helmet would fail from the adhesive region under tensile loading.

3.3.3. Analyses of Most Critical Regions in accordance with the Impact Probability

According to Figure 67, during an accident, the damage on the helmet will most probably occur on the right chin. Therefore, an analysis was conducted to observe the stress distribution when a force was applied on the chin. The results are presented in Figure 74.

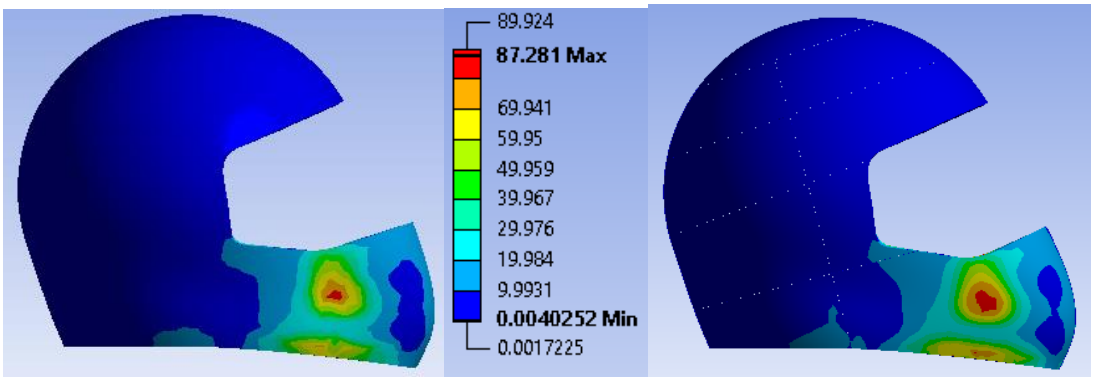

(a) Whole helmet (b) Partitioned and glued helmet

Figure 74. Equivalent stress result (MPa) in case of impact on chin

Results of numerical analysis revealed that when the impact was applied, the helmet failed from the center of the impact. When the stress distributions over all of the adhesive layers were investigated, it was observed that the maximum stress and strain values were below the critical point of the adhesive; therefore, no failing from the adhesive layer occurred.

In terms of the performances of both helmets, it can be concluded that, the partitioning and bonding process only caused a 2 MPa increase in maximum stress value; yet it did not critically effect the strength of the object while the failure did not occur in adhesive layer.

When the probabilities in Figure 67 are observed, it can be seen that the second most critical region after the chins was the left upper part, with a percentage of 10.1. An analysis was conducted for this region as well. For this analysis, the magnitude of the applied force was chosen such that the resultant maximum stress value stayed below the yield strength of the PLA material. As a result, the failure of the helmet would be prevented and the behavior of the adhesive layer could be observed. The equivalent stress distribution result of the helmet is presented in Figure 75. As it can be interpreted from Figure 75, the impact caused no failure on the helmet, while the maximum stress was lower than the yield strength of the PLA, which was 70.71 MPa.

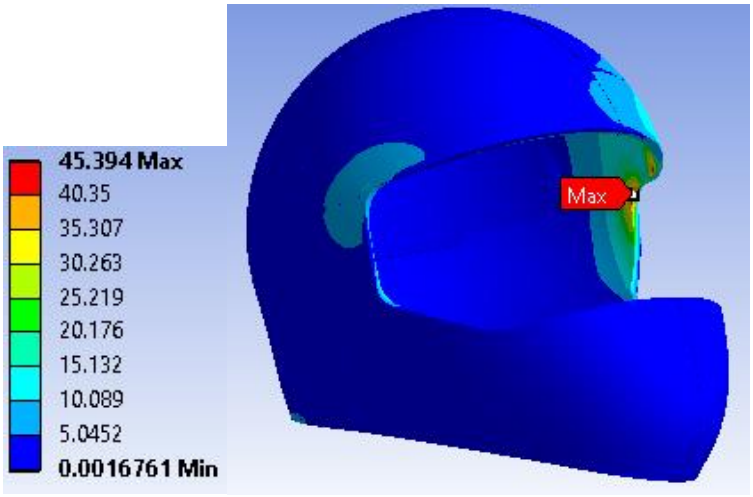

Figure 75. Equivalent stress distribution (MPa) on the helmet

On the other hand, when the stress distribution on the critical adhesive region was examined, it was observed that the maximum stress value occurred at the edge of the adhesive layer. The equivalent stress distribution result is shown in Figure 76 and as it can be seen from the figure, the maximum stress was 38 MPa which was more than 3 times greater than the yield strength of the adhesive. Therefore, failing occurred from the adhesive region. This failure may be avoided by choosing the partitioning regions differently.

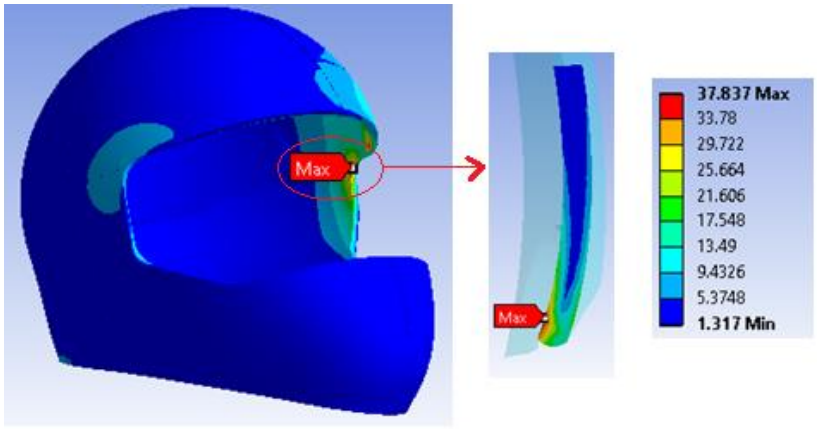

Figure 76. Equivalent stress distribution (MPa) on the most critical adhesive region from top view

To avoid the failure of the adhesive region, the two parts can be united and printed as one part. By doing that, the adhesive region was eliminated and therefore the strength of the critical region was increased. The united parts can be seen in Figure 77.

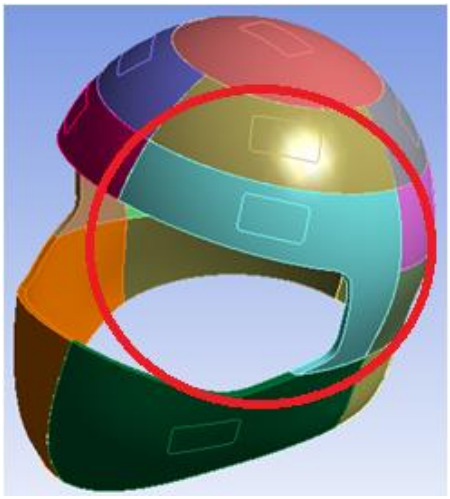

Figure 77. The united parts

The dimensions of the united part were checked and it was concluded that it could still fit into the printing volume of the 3D printer. When the analysis was repeated by using the same force, similar results with Figure 75 were obtained. The equivalent stress results for this case are presented in Figure 78. It can be seen that, this time in

the critical region there exist no adhesive and the maximum stress value was below the yield strength of PLA. Moreover, when the maximum stress values over the other adhesive regions were investigated, it was observed that the maximum stress on the adhesive regions was 3.89 MPa, which was lower than the critical value of 502CAE. Therefore, it can be concluded that by not dividing the critical region into two pieces and keep it as one part, the failure from the adhesive region was prevented under same loading conditions.

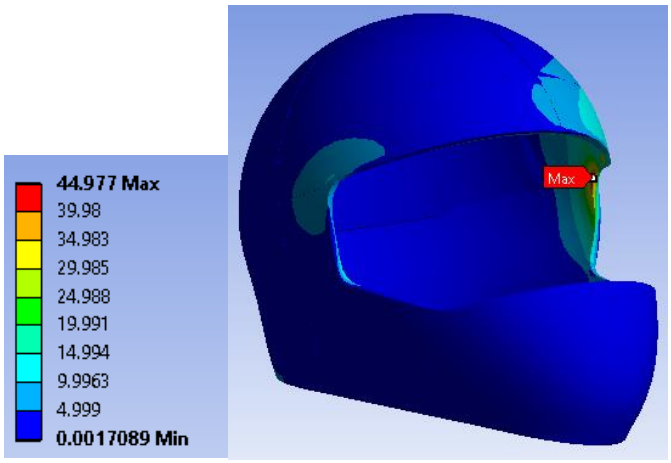

Figure 78. Equivalent stress distribution (MPa) on the helmet after two parts were united

3.3.4. Analysis of Non-Critical Region in accordance with Impact Probability

As another example, one of the regions having lower probability was numerically analyzed. In this case, the impact load was applied on the back, for which the probability of impact was 1.8%. The equivalent stress results for the whole and partitioned and bonded helmet are presented in Figure 79.

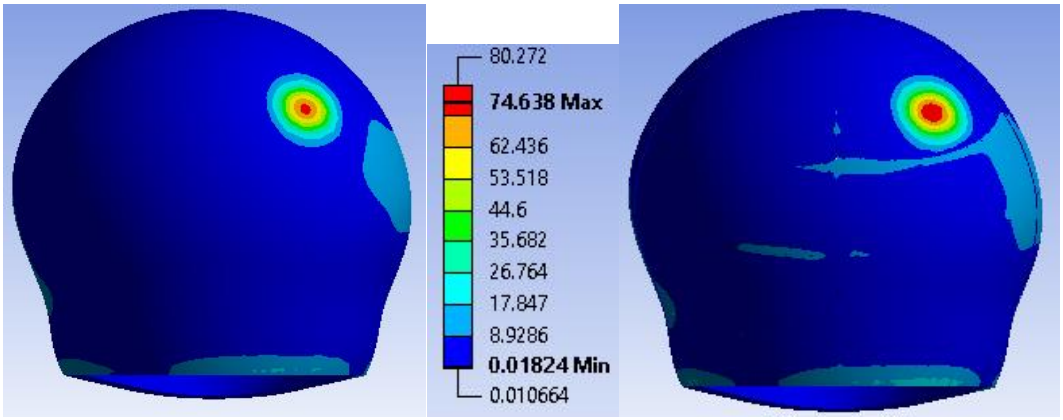

(a) Whole helmet (b) Partitioned and glued helmet

Figure 79. Equivalent stress results (MPa) in case of impact on the upper back part

When examining Figure 79, several conclusions can be made. Firstly, for the whole helmet model, the effect of the impact was regional. Secondly, the impact caused a stress distribution on the adhesive layer for the partitioned and glued helmet. Thirdly, when the maximum stresses for both helmets were compared, it can be seen that for the whole helmet the maximum stress is lower than the partitioned and glued helmet. However, the difference between the maximum stresses was about 7%. To find out whether a failure in adhesive region occurred or not, the stress distributions over all of the adhesive layers were investigated. It was observed that the maximum stress on the adhesive layer was found as 7.4 MPa, which was lower than the yield strength of 502CAE.

3.3.5. Partitioning Considerations

The partitioning for the helmet could have been done by many different methods. In this study, the 17 regions of Otte's diagram were used for partitioning the helmet. One of the reasons for that was to use the data of most probably damaged region during an accident.

In this section, two methods that can be used for partitioning the helmet are explained and analyzed. For the first method, in order to find out the most critical region, the analyses were conducted for each region separately and the solutions were combined

together. In other words, the same analysis was conducted for each region and then combined together by multiplying their impact probabilities to decide the most critical region. The analyses were conducted by using a whole helmet and partitioned and bonded helmet, and the effect of partitioning was investigated. The results are presented in Figure 80.

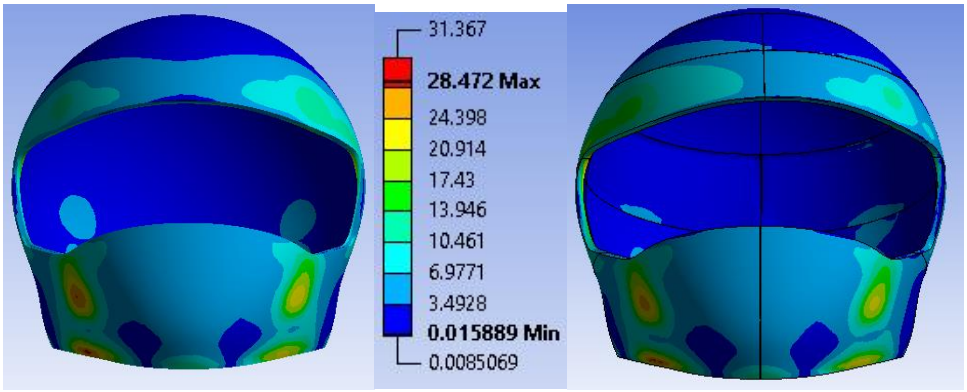

(a) Whole helmet (b) Partitioned and glued helmet

Figure 80. Equivalent stress distribution (MPa) on helmet by using probabilities

It can be clearly seen from Figure 80 that the region on which greatest stress occurred was right chin. This result matches with Otte's percentages. This maximum stress was smaller than the yield strength of PLA material; therefore, it can be said that helmet would not fail. Moreover, when the equivalent stress values were investigated for all the adhesive layers, it was seen that all of them were below the yield strength of the adhesive. In other words, adhesive layer would not fail as well. In addition, when the results of whole and partitioned helmets were compared, a significant difference between them can be seen as the increase in maximum stress value, which was about 9%. In conclusion, the results showed that the performance of the partitioned and bonded helmet was closer to the whole helmet. Another conclusion that can be drawn from this analysis is that due to its higher impact probability, right chin of the helmet was the most critical region. While partitioning the helmet prior to manufacturing, one can consider this part as the most critical part and do the partitioning such that the

strength of the part was not reduced. For instance, dividing this part into two from the middle may not be reasonable partitioning.

As the second method for partitioning, the probabilities for all regions can be chosen as equal. Thus, the actual most critical region can be found.

An analysis was done by taking the effect of each region as equal and the equivalent stress results are presented in Figure 81.

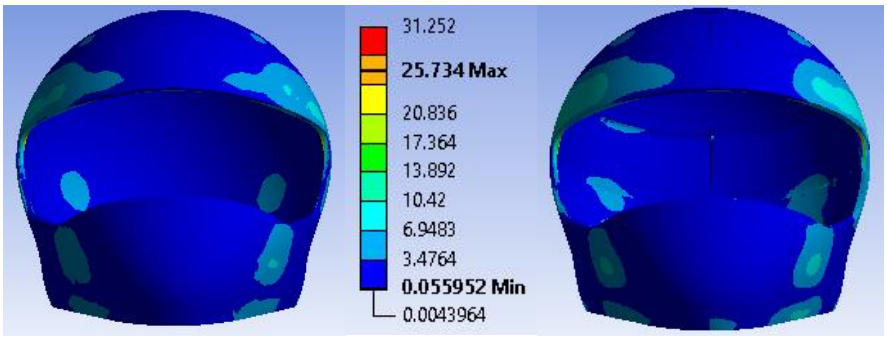

(a) Whole helmet (b) Partitioned and glued helmet

Figure 81. Equivalent stress (MPa) distribution on helmet by using equal percentages

As it can be seen from Figure 81, when the probabilities were taken as equal the most critical region found to be the edge of the helmet. Moreover, the difference between the maximum stress values of whole and partitioned helmet was found about 18%.

By investigating the results of this analysis, it can be concluded that, while partitioning the helmet, the parts near the edge should be stronger and should be left as undivided if possible.

The analysis was repeated for the PLA properties found by Song et. al [14] in their study, by using the second method. The equivalent stress results for whole helmet and partitioned helmet are presented in Figure 82.

When the figure was investigated, it can be observed that both helmets showed similar behavior. The main difference between these results and the results which were found previously, is the values of maximum stress. Rather than that, the stress distributions were similar. The reason for the increase in the maximum stress may be the larger elastic modulus value that Song et al. calculated for PLA.

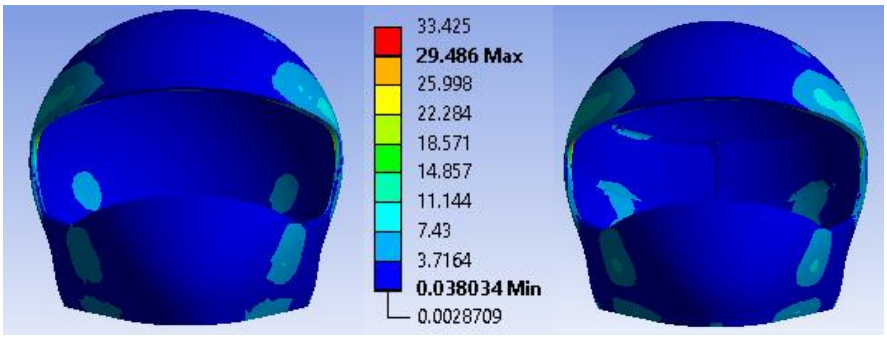

(a) Whole helmet (b) Partitioned and glued helmet

Figure 82. Equivelant stress result (MPa) by using PLA properties in literature

CHAPTER 4

CONCLUSIONS AND FUTURE WORK

4.1. Summary

In this study, mechanical characteristics of 3D printed PLA objects were investigated both experimentally and numerically. After showing that numerical analyses results were similar with the experimental results, the know-how was used for a case study.

In Chapter 2, the experiments that were done to observe the behavior of the PLA material under compression and tensile loading were explained in detail. The specimens were printed by Hüseyin Enes Salman and Cem Baykal in the METU ME vibration laboratory. The tests were done under the guidance of Servet Şehirli in the METU ME material testing laboratory. The effect of infill percentage on the mechanical characteristics of PLA was investigated for compression loading. For this purpose, specimens with two different infill percentages were produced. One was chosen as 20%, which was the default value of the 3D printer, and the other one was chosen as 100%. The tensile tests were done only by using 20% infill specimens. After that, photostress tests were conducted to observe the stress distribution on the 100% infill compression test specimen and 20% infill tensile test specimen. The test results were presented in Chapter 2 and they were compared with the findings of similar studies done in literature. As the second part of Chapter 2, numerical simulations of the compression and tensile tests were done. Numerical modelling was explained in detail and the results were presented. In Section 2.3, the results were compared with the experimental re-

sults. In Section 2.3.3, for both compression and tensile test specimens, the mechanical properties for different infill percentages were estimated by using the properties of the bulk specimens.

In Chapter 3 a case study was presented. The aim of this case study was to demonstrate that a partitioned and bonded object show similar performance with a whole object. Therefore, a motorcycle helmet was modelled in order to simulate an application of 3D printer in real life. Since helmet is a large object in order to print it with home-use 3D printer, it should be partitioned to smaller pieces and glued together. Simulations were conducted to see the effect of this process on the strength of the helmet. While modelling the helmet, results obtained from the experiments were used. The numerical analyses results were then repeated by using PLA material properties available in the literature and both results were compared.

4.2. Conclusions

In this study 3D printed PLA specimens were tested, the tests were numerically modelled and the found mechanical properties of the PLA was used in a case study. As a result of this study, following conclusions can be made.

For the compression tests, even though all of the specimens were produced at the same time, from the same spool of filament and under the same conditions, difference in failure mode of specimens were observed. The 20% infill specimens showed discrepancies in the failing regions. Moreover, when the stress-strain plot of each specimen was investigated, different behaviors were observed for some of the specimens. From these results, it can be concluded that, for lower infill percentages, any small difference in the infill pattern result in variation in the mechanical property of the material. Moreover, the infill pattern of the object is highly effected from the sensitivity of the 3D printer.

Results of compression tests done by using 100% infill specimens showed that failure mode and regions were similar for all specimens. The small differences may result from the places of air gaps within the specimens.

When the results of 20% and 100% infill specimens are compared, it was observed that 100% infill specimens were about 4 times stronger than the 20% infill specimens. Therefore, while printing the objects, choosing the infill percentage as 100 will result in parts with higher quality.

During the numerical analyses, the results of the tests were used to define the mechanical properties of the PLA. With numerical analyses the tests were simulated and the results showed similarity with the experimental results with a difference of maximum 10%.

The tensile tests were done by using five 20% infill specimens. Different fracture locations for each specimen were observed while during the tensile tests the object would fail from the weakest region. The difference between the dimensions of the specimens results from the sensitivity of the 3D printer as well.

The tensile tests were modelled by taking the fracture point from the tests as references. The numerical analyses results showed similarity with the experimental results; however, the fracture point for the specimens were reached after applying a displacement which was about 20% greater than the real displacement value. This result indicates that the model used in numerical analyses was stronger than the real specimen. In real life while printing the specimens, there are many conditions affecting the strength of the parts. Even a small variation in the infill pattern of the specimen can result in different mechanical properties. The observations done in tensile test results actually support this claim. In numerical analyses, the specimens were assumed to have perfect dimensions and it is not possible to model these imperfections.

Photostress method can be used to observe the strain distribution on a 3D printed object. However, in order to do that proper coating material and reflective paint should be used.

A case study was presented as an example of application of home-use 3D printers. A motorcycle helmet was partitioned and the sub-parts were bonded together by using a commercial adhesive. Numerical analyses were done for the whole and partitioned helmet. The results showed similarity in performance of both helmets. Nevertheless, it was shown that the results were highly dependent on the partitioning region and the used adhesive.

4.3. Future Work

During this study some assumptions were made and some simplifications were done and the results can be improved by doing the numerical analyses without these assumptions or simplifications in future work.

First of all, in this study the mechanical properties of the adhesion layer were chosen to be isotropic, which creates a limitation. As a future work, anisotropic material properties can be calculated by experiments and can be assigned to the adhesive material for the numerical analyses.

Secondly, the effect of printing direction on the strength of the final parts was not considered, although the printing direction plays a role in the strength of the object. This was difficult to model especially for the case study, while the printing direction for each of the sub-parts should be considered prior to modelling. As future work parts can be produced for different printing directions and the effect of this can be investigated on the behavior of the whole object after bonding of the sub-parts.

Some improvements can be done as an addition of work presented by this study. First example, in this study, photostress method was only used to observe the strain distribution and no detailed quantitative calculations were done. Photostress method can be used especially on the complex 3D printed parts, to investigate the critical regions and the strain values of the regions can be calculated.

Secondly, in this thesis, the helmet was partitioned into small parts and after partitioning, the obtained interfacial surfaces were smooth. When smooth interfaces are glued together, the strength of the final part depends only on the strength of the adhesive

surface. However, if notched surface is created as the adhesive surface and then the two parts are glued together, the strength of the final object should increase. The notched surface increases the surface area that touches together and also improves the strength in one more direction. The notched surface can be easily obtained by 3D printing. As a future work, this method can be tested and the results can be compared.

Finally, for the partitioning of the large objects, different methods can be used. The most meaningful method would be doing the partitioning by considering the stress distribution within the object. For the helmet, the critical regions were determined by using two different methods. As future work these critical regions can be strengthened and the effect of partitioning from different regions on the strength of the object can be observed.

REFERENCES

[1] K. Bassett, R. Carriveau, D.S.K. Ting, 3D printed wind turbines part 1: Design considerations and rapid manufacture potential, Sustain. Energy Technol. Assessments. 11 (2015) 186–193. doi:10.1016/j.seta.2015.01.002.

[2] K.S. Boparai, R. Singh, H. Singh, Development of rapid tooling using fused deposition modeling: a review, Rapid Prototyp. J. 22 (2016) 281–299. doi:10.1108/RPJ-04-2014-0048.

[3] K. Brans, 3D printing, a maturing technology, IFAC, 2013. doi:10.3182/20130522-3-BR-4036.00112.

[4] S. Hwang, E.I. Reyes, K. sik Moon, R.C. Rumpf, N.S. Kim, Thermo-mechanical Characterization of Metal/Polymer Composite Filaments and Printing Parameter Study for Fused Deposition Modeling in the 3D Printing Process, J. Electron. Mater. 44 (2015) 771–777. doi:10.1007/s11664-014-3425-6.

[5] S.F. Costa, F.M. Duarte, J.A. Covas, Thermal conditions affecting heat transfer in FDM/FFE: a contribution towards the numerical modelling of the process, Virtual Phys. Prototyp. 10 (2014) 35–46. doi:10.1080/17452759.2014.984042.

[6] S. Singh, R. Singh, Fused deposition modelling based rapid patterns for investment casting applications: a review, Rapid Prototyp. J. 22 (2016) 123–143. doi:10.1108/RPJ-02-2014-0017.

[7] J.L. Chulilla Cano, The Cambrian Explosion of Popular 3D Printing, Int. J. Interact. Multimed. Artif. Intell. 1 (2011) 30. doi:10.9781/ijimai.2011.145.

[8] T. Rayna, L. Striukova, From rapid prototyping to home fabrication: How 3D

printing is changing business model innovation, Technol. Forecast. Soc. Change. 102 (2016) 214–224. doi:10.1016/j.techfore.2015.07.023.

[9] O.A. Mohamed, S.H. Masood, J.L. Bhowmik, Experimental investigation of time-dependent mechanical properties of PC-ABS prototypes processed by FDM additive manufacturing process, Mater. Lett. 193 (2017) 58–62. doi:10.1016/j.matlet.2017.01.104.

[10] J.E. Renaud, J.F. Rodriguez, J.P. Thomas, Modeling the Mechanical Behaviour of Fused Deposition acrylonitrile-butadiene styrene polymer components, Dep. Aerosp. Mech. Eng. PhD Disser (1999).

[11] C. Casavola, A. Cazzato, V. Moramarco, C. Pappalettere, Orthotropic mechanical properties of fused deposition modelling parts described by classical laminate theory, Mater. Des. 90 (2016) 453–458. doi:10.1016/j.matdes.2015.11.009.

[12] S. Ziemian, M. Okwara, C.W. Ziemian, Tensile and fatigue behavior of layered acrylonitrile butadiene styrene, Rapid Prototyp. J. 21 (2015) 270–278. doi:10.1108/RPJ-09-2013-0086.

[13] J. Cantrell, S. Rohde, D. Damiani, R. Gurnani, L. Disandro, J. Anton, A. Young, A. Jerez, D. Steinbach, C. Kroese, P. Ifju, Experimental Characterization of the Mechanical Properties of 3D-Printed ABS and Polycarbonate Parts, Adv. Opt. Methods Exp. Mech. 3 (2016) 89–105. doi:10.1007/978-3-319-41600-7_11.

[14] Y. Song, Y. Li, W. Song, K. Yee, K.-Y. Lee, V.L. Tagarielli, Measurements of the mechanical response of unidirectional 3D-printed PLA, Mater. Des. 123 (2017) 154–164. doi:http://dx.doi.org/10.1016/j.matdes.2017.03.051.

[15] T. Letcher, Imece2014-39379 Material Property Testing of 3D-Printed Specimen, (2014) 1–8.

[16] J.M. Chacón, M.A. Caminero, E. García-Plaza, P.J. Núñez, Additive

manufacturing of PLA structures using fused deposition modelling: effect of process parameters on mechanical properties and their optimal selection, Mater. Des. 124 (2017) 143–157. doi:10.1016/j.matdes.2017.03.065.

[17] M.K. Agarwala, R. Van Weeren, R. Vaidyanathan, N. Langrana, a Safari, S.H. Garofalini, S.C. Danforth, Structural Ceramics by Fused Deposition of Ceramics, Solid Free. Fabr. Symp. (1995) 1–8.

[18] R.W. Gray Iv, D.G. Baird, J.H. Bøhn, Rapid Prototyping Journal Effects of processing conditions on short TLCP fiber reinforced FDM parts, Rapid Prototyp. J. Iss Rapid Prototyp. J. Iss Rapid Prototyp. J. Iss Rapid Prototyp. J. 4 (1998) 14–25. doi:10.1108/13552549810197514.

[19] M. Nikzad, S.H. Masood, I. Sbarski, Thermo-mechanical properties of a highly filled polymeric composites for Fused Deposition Modeling, Mater. Des. 32 (2011) 3448–3456. doi:10.1016/j.matdes.2011.01.056.

[20] Z. Weng, J. Wang, T. Senthil, L. Wu, Mechanical and thermal properties of ABS/montmorillonite nanocomposites for fused deposition modeling 3D printing, Mater. Des. 102 (2016) 276–283. doi:10.1016/j.matdes.2016.04.045.

[21] L. Lu, A. Sharf, H.S. Zhao, Y. Wei, Q.N. Fan, X.L. Chen, Y. Savoye, C.H. Tu, D. Cohen-Or, B.Q. Chen, Build-to-Last: Strength to Weight 3D Printed Objects, Acm Trans. Graph. 33 (2014) 1–10. doi:Artn 97\r10.1145/2601097.2601168.

[22] A. Kantaros, D. Karalekas, Fiber Bragg grating based investigation of residual strains in ABS parts fabricated by fused deposition modeling process, Mater. Des. 50 (2013) 44–50. doi:10.1016/j.matdes.2013.02.067.

[23] C. Casavola, A. Cazzato, V. Moramarco, G. Pappalettera, Residual stress measurement in Fused Deposition Modelling parts, Polym. Test. 58 (2017) 249–255. doi:10.1016/j.polymertesting.2017.01.003.

[24] L. Luo, I. Baran, S. Rusinkiewicz, W. Matusik, Chopper: partitioning models

into 3D-printable parts, ACM Trans. Graph. 31 (2012) 1–9. doi:10.1145/2366145.2366148.

[25] J. Hao, L. Fang, R.E. Williams, An efficient curvature-based partitioning of large-scale STL models, Rapid Prototyp. J. 17 (2011) 116–127. doi:10.1108/13552541111113862.

[26] P. Song, Z. Fu, L. Liu, C. Fu, Printing 3D objects with interlocking parts, Comput. Aided Geom. Des. 35–36 (2015) 137–148. doi:10.1016/j.cagd.2015.03.020.

[27] M. Mirkhalaf, F. Barthelat, Design , 3D printing and testing of architectured materials with bistable interlocks, Extrem. Mech. Lett. 11 (2017) 1–7. doi:10.1016/j.eml.2016.11.005.

[28] B.J. Doyle, J. Killion, A. Callanan, Use of the photoelastic method and finite element analysis in the assessment of wall strain in abdominal aortic aneurysm models, J. Biomech. 45 (2012) 1759–1768. doi:10.1016/j.jbiomech.2012.05.004.

[29] R.B. Judge, J.E. a Palamara, R.G. Taylor, M.S. Helen, J.G. Clement, of a Dog Skull Loaded in Vitro, 90 (2003).

[30] L.J. Jankowski, J. Jasieńko, T.P. Nowak, Experimental assessment of CFRP reinforced wooden beams by 4-point bending tests and photoelastic coating technique, Mater. Struct. 43 (2010) 141–150. doi:10.1617/s11527-009-9476-0.

[31] B. Çevik, A.Ö.Y. Özçatalbaş, Köşe Kaynaklarında Oluşturulan Gerilmelerin Fotoelastisite Yöntemiyle Analizi, (2011) 16–18.

[32] P. Specimens, Compressive Properties of Rigid Plastics 1, Annu. B. ASTM Stand. i (2008) 1–8. doi:10.1520/D0695-15.2.

[33] A.K. Sood, R.K. Ohdar, S.S. Mahapatra, Experimental investigation and empirical modelling of FDM process for compressive strength improvement, J. Adv. Res. 3 (2012) 81–90. doi:10.1016/j.jare.2011.05.001.

[34] C. Ziemian, M. Sharma, S. Ziemian, Anisotropic mechanical properties of ABS parts fabricated by fused deposition modelling, Mech. Eng. (2012) 159–180. doi:10.5772/34233.

[35] M. Ast, D638, Standard test method for tensile properties of plastics, TF_~ VFING HOOP TENSlLE l'REN …. (2013) 1–16. doi:10.1520/D0638-10.1.

[36] W. Wu, P. Geng, G. Li, D. Zhao, H. Zhang, J. Zhao, Influence of layer thickness and raster angle on the mechanical properties of 3D-printed PEEK and a comparative mechanical study between PEEK and ABS, Materials (Basel). 8 (2015) 5834–5846. doi:10.3390/ma8095271.

[37] V.P.G. Inc, Introduction to Stress Analysis by the PhotoStress ® Method by by TN-702-2 the PhotoStress, (2005).

[38] T.Q. Sm, C.T. Cylinder, D. Computer, ME 457 Experimental Solid Mechanics (Lab) Computerized Thin Cylinder Experiment, (n.d.) 2–5.

[39] S. Farah, D.G. Anderson, R. Langer, Physical and mechanical properties of PLA , and their functions in widespread applications — A comprehensive review ☆, Adv. Drug Deliv. Rev. 107 (2016) 367–392. doi:10.1016/j.addr.2016.06.012.

[40] A. Xie, MSDS Report, Regulation. 2010 (2010) 5–11.

[41] 3dmatter, What is the influence of infill %, layer height and infill pattern on my 3D prints?, (2015). http://my3dmatter.com/influence-infill-layer-height-pattern/.

[42] F.A.O. Fernandes, R.J. Alves De Sousa, Motorcycle helmets - A state of the art review, Accid. Anal. Prev. 56 (2013) 1–21. doi:10.1016/j.aap.2013.03.011.

[43] L. Di Landro, G. Sala, D. Olivieri, Deformation mechanisms and energy absorption of polystyrene foams for protective helmets, Polym. Test. 21 (2002) 217–228. doi:10.1016/S0142-9418(01)00073-3.

[44] C. of I. into H.I. and M. Services, Interim Report, (2001) 1–83.

[45] National Highway Traffic Safety Administration, Motorcycle Safety, 2008 (1999).

[46] Grabcad, No Title, (2016). https://grabcad.com/library/tag/helmet.

[47] E. (Snell C.E. and E.D. Becker, Snell, 2016.

[48] F.M. Shuaeib, a. M.S. Hamouda, R.S. Radin Umar, M.M. Hamdan, M.S.J. Hashmi, Motorcycle helmet, J. Mater. Process. Technol. 123 (2002) 406–421. doi:10.1016/S0924-0136(02)00048-1.